Supporting Information

The Construction of Multifunctional Solid Electrolytes Interlayer for Stabilizing Li_6PS_5Cl-based All-Solid-State Lithium Metal Batteries

Ya Chen,§[ab] Xin Gao,§[b] Zheng Zhen,§[b] Xiao Chen,[c] Ling Huang,[e] Deli Zhou,[c] Tengfei Hu,[h] Bozhen Ren,[f] Runjing Xu,[g] Jiayi Chen,[b] Xiaodong Chen,*[c] Lifeng Cui,*[a] Guoxiu Wang*[d]

[a] Smart Materials for Architecture Research Lab, Innovation Center of Yangtze River Delta, Zhejiang University, Jiashan, Zhejiang 314100, China. E-mail: lifeng.cui@gmail.com

[b] College of Smart Energy, Shanghai Jiao Tong University, Shanghai, 200240, China

[c] Department of Mechanical Engineering, City University of Hong Kong, Tat Chee Avenue, Kowloon, Hong Kong, China. E-mail: xche24@cityu.edu.hk

[d] Center for Clean Energy Technology, School of Mathematical and Physical Science, Faculty of Science, University of Technology Sydney, Sydney, New South Wales 2007, Australia. E-mail: Guoxiu.Wang@uts.edu.au

[e] School of Physical Science and Technology, ShanghaiTech University, Shanghai, 201210, China

[f] School of mathematic, South China University of Technology, 381 Wushan Road, Tianhe District, Guangzhou City, 510641, China

[g] School Department of Materials Science, Fudan University, Shanghai, 200433, China

[h] Key Laboratory of Inorganic Functional Materials and Devices, Shanghai Institute of Ceramics, Chinese Academy of Sciences, 588 Heshuo Road, Jiading District, Shanghai, 201800, China

§ These authors contributed to this work equally.

1. Experimental section

1.1 Materials preparation

All the preparation processes were performed in an argon-filled glovebox (O_2< 0.1 ppm, H_2O < 0.1 ppm).

1.1.1 The preparation of Li_6PS_5Cl (LPSC) Electrolyte:

Li_2S (99.9%), P_2S_5 (99.9%) and LiCl (99.9%) were weighed and mixed in a molar ratio of 5:1:2, then the obtained mixture was ball-milled at 600 rpm for 10 h in a ZrO_2 vial with ZrO_2 balls. The resulting powders were annealed at 550 °C for 6 hours with a heating rate of 5 °C min^{-1}.

1.1.2 The preparation of $Li_{1.3}Al_{0.3}Ti_{1.7}(PO_3)_4$ (LATP) Electrolyte:

The preparation of ceramic LATP via a solution method. The stoichiometric amounts of high-purity TiO_2 (99%), nanometer-sized Al_2O_3 (99.9%), $LiOH·H_2O$ (99.99%) and H_3PO4 (85%) were weighed and mixed for 1 h with purified water as solvent. After being dried at 180°C overnight, the LATP precursor powders were heated at 700 °C for 4 h, followed by another ball milling and heating at 800°C for 12 h to obtain pure LATP powder.

1.1.3 The preparation of $LiCoO_2$ composite cathode:

The Li_3PO_4 coated $LiCoO_2$ powder was purchased from Xiamen Tungsten Co., Ltd. And the $LiCoO_2$ (LCO) powder, LPSC powder and Super P were weighed in a mass ratio of 70:25:5, and then mixed for 10 minutes using mortar and pestle.

1.1.4 The preparation of LPSC-LATP composite powder:

The LPSC-LATP composite electrolytes with the different component mass ratios from 9:1 to 4:6 (labeled as 9S-1O, 8S-2O,7S-3O, 6S-4O, 5S-5O and 4S-6O respectively) were synthesized through ball-milling at 300 rpm for 4h in a ZrO_2 vial with ZrO_2 balls.

And the ball/material ratio were 18:1.

1.2 Cells assembly

All assembly processes were performed in an argon-filled glovebox (O_2< 0.1 ppm, H_2O < 0.1 ppm) to avoid side reactions between materials and air.

1.2.1 The assembly of blocking SS/LPSC-LATP/SS symmetric cell:

200 mg LPSC-LATP composite powder were placed into the mold with a diameter of 10 mm, followed by cold pressing at 300 MPa for 5 minutes. Afterwards, two stainless steel discs were pressed on both sides.

1.2.2 The assembly of blocking Au/LATP/Au symmetric cell:

The LATP powder was pressed into pellet and sintered at 800^{o}C for 12 h in ambient atmosphere. And the white homogeneous LATP ceramics with a diameter a 15 mm and thickness of about 1 mm were obtained. Afterwards, the Au layers were established on both sides of LATP pellet by ion sputtering

1.2.3 The assembly of blocking SS/LPSC/SS symmetric cell and nonblocking Li/LPSC/Li symmetric cell:

200 mg LPSC powder were placed into the mold with a diameter of 10 mm, followed by cold pressing at 300 MPa for 5 minutes. Afterwards, two stainless steel discs were pressed on both sides and thus the block Au/LPSC/Au symmetric cell was assembled. Likewise, the stainless steel discs were replaced by Li foils for the assembly of Li/LPSC/Li symmetric cell.

1.2.4 The assembly of nonblocking Li/LPSC/LPSC-LATP/LPSC/Li symmetric cell:

100 mg LPSC-LATP composite powder were placed into the mold with a diameter of 10 mm followed by cold pressing at 50 MPa. Then 50 mg of LPSC powder were evenly spread on both sides, respectively, followed by another cold pressing at 300 MPa

for 5 minutes to form LPSC/LPSC-LATP/LPSC electrolyte with sandwich structure. Finally, Li foils were pressed on both sides.

1.2.5 The assembly of Li/LPSC/LPSC-LATP/LPSC/LCO full cell:

100 mg LPSC-LATP composite powder were placed into the mold with a diameter of 10 mm followed by cold pressing at 50 MPa. Then 50 mg of LPSC powder were evenly spread on both sides, respectively, followed by cold pressing at 100 MPa for 5 minutes to form LPSC/LPSC-LATP/LPSC electrolyte with sandwich structure. The prepared LCO composite cathode powder was spread on the one side evenly followed by cold pressing at 300 MPa for 5 minutes. The mass loadings of LCO are controlled to be 8 mg cm^{-2} and 10 mg cm^{-2}, which would be marked at relevant graphs and tables. Finally, the Li foil was pressed on another side.

1.3 Materials characterizations

1.3.1 X-ray diffraction (XRD):

XRD measurements were carried out over a 2θ range of 10−70 ° (Rigaku Utima IV) with a Cu Kα line as radiation source. And the samples were sealed by Kapton films to avoid the side reactions in O_2 and moisture from the air.

1.3.2 X-ray photoelectron spectroscopy (XPS):

X-ray photoelectron spectroscopy was carried out using a spectrometer (Thermo ESCALAB, 250xi). Monochromatic Al Kα radiation was used for analysis (3000 eV). The power of the X-ray source was 50 W, and the beam voltage was 15 kV. The beam diameter was 900 μm. Depth profiling was performed using Ar^+ ions (soft sputtering with 0.5 kV) to clean the surface and to avoid misinterpretations due to reactions that occur only on the surface. The rasterized area was (6 × 6) mm^2. The samples were

transferred to the analysis chamber in an argon-filled transfer bin in order to avoid air exposure.

1.3.3 Solid-state ^{7}Li NMR measurements:

^{7}Li static and MAS solid-state NMR measurements were performed on a Bruker AVANCE NEO 400WB spectrometer.

Additionally, the morphologies of the samples were characterized by a Hitachi S-3400 scanning electron microscope. The *operando* Raman spectroscopy measurements were performed with a Renishaw inVia Qontor instrument. The wavenumber range for collecting Raman spectra is from 100 to 1500 cm^{-1}.

1.4 Electrochemical measurement

1.4.1 Electrochemical impedance spectroscopy (EIS):

EIS measurements were conducted at frequencies from 1 MHz to 0.1 Hz with the AC amplitude of 10 mV on an autolab electrochemical workstation (Autolab PGSTAT 302N). Activation energies were determined by temperature-dependent EIS measurements using 5 or 10 °C temperature steps between 20 and 70 °C. Prior to the measurement, the system was kept at the chosen temperature for over 2 hours. And the calculation is based on the Arrhenius equation $\sigma T = Aexp(-Ea/kT)$, in which σ is the ionic conductivity, T is the temperature in Kelvin, A is the pre-exponential factor, k as the Boltzmann constant, E_a is the activation energy of Li^+ hopping between two adjacent sites.

1.4.2 Cycling performance:

The galvanostatic polarization and cycling measurements were conducted using a Neware battery test system (China) and a multichannel battery testing system (LAND CT2001A).

1.5 DFT calculation details

The first-principles calculations are performed in the framework of the density

functional theory with the projector augmented plane-wave method, as implemented in the Vienna ab initio simulation package.[1] The generalzied gradient approximation of Perdew, Burke, and Ernzerhof (PBE) is employed for the exchange-correlation potential.[2] The long range van der Waals interaction is described by the DFT-D3 approach.[3] The Li(001)/Li_6PS_5Cl(100) heterostructure is composing of 144 Li, 12 P, 60 S, and 12 Cl atoms; the Li(001)/$Li_{1.3}Al_{0.3}Ti_{1.7}(PO_4)_3$(012) is composing of 36 P, 144 O, 160 Li, 20 Ti, and 4 Al. The cut-off energy for plane wave is set to 500 eV. The converged conditions for ionic and electronic optimizations are chosen as 0.03 eV/Å and 1×10^{-5} eV. The Brillouin zone integration is performed using a 2×2×1 k-mesh for Li(001)/Li_6PS_5Cl(100), and a 3×1×1 k-mesh for Li(001)/$Li_{1.3}Al_{0.3}Ti_{1.7}(PO_4)_3$(012).

1.6 Phase field simulation details

The mechanical electrochemical model constructed by simulating the battery is based on the phase field method,[4] which is coupled with four major equations including phase field equation, concentration field equation, electrostatic equation, and mechanical equilibrium equation. Write the following equation using COMSOL6.2 custom partial differential equation for simulation.

Phase field equation：

$$\frac{\partial \xi}{\partial t} = -\mathrm{L}_\sigma\left(g'(\xi) + f'_{grad}(\xi) + f'_{els}(u,\xi)\right) - \mathrm{L}_\eta h'(\xi)\left(e^{\frac{(1-\alpha)F\eta}{RT}} - \frac{c_{Li^+}}{c_0}e^{\frac{-\alpha F\eta}{RT}}\right)$$

ξ is a phase field variable ranging from 0 to 1, where 0 represents the liquid e lectrolyte and 1 represents the solid electrode. $g(\xi) = w\xi^2(1-\xi)^2$ is the arbitrar y double well potential function, where W is barrier. $h(\xi) = \xi^3(6\xi^2 - 15\xi + 10$) is the interpolation function, which promise efficiency of Butler-Volmer at the

interface. α and η are charge transfer coefficient and electric overpotential respe ctively. R, T, F, L_σ, L_η, u and c_{Li^+} represent molar gas constant, temperature, Faraday constant, interface migration rate, reaction related constant, displacemen t and Li^+ concentration, respectively. For $f_{els}(u,\xi)=\frac{1}{2}C_{ijkl}\varepsilon_{ij}^{E}\varepsilon_{kl}^{E}$, the ε_{ij}^{E}、$\varepsilon_{kl}^{E}$are elastic strain tensors, and C_{ijkl} is local phase dependent stiffness tensor. The $f_{grad}(\xi)=\frac{1}{2}\kappa_0[1+\delta\cos(\omega\theta)\nabla^2\xi]$ represents gradient energy density, wher e κ_0, δ, and ω are gradient energy coefficient，strength of anisotropy and anisotropic patterns respectively. Additionally, θ represents angle between normal vectors and the reference axis interface.

Concentration field equation：

$$\frac{\partial c_{Li^+}}{\partial t}=\nabla\cdot\left(D_{Li^+}\nabla c_{Li^+}+D_{Li^+}c_{Li^+}\frac{F}{RT}\nabla\phi e\right)-c_{Li}\frac{\partial\xi}{\partial t}$$

where D_{Li^+}, c_{Li^+} and ϕe represent the diffusion coefficient of Li^+, initial concentration of electrode and potential of electrolyte. To be mentioned, the diffusion and electromigration are simultaneously considered here.

Electrostatic potential distribution equation：

$$\nabla\cdot\left(\sigma_{eff}\nabla\phi_{Li}\right)=Fc_{Li}\frac{\partial\xi}{\partial t}$$

where $\sigma_{eff}=h(\xi)\sigma_{Li}+(1-h(\xi))\sigma_e$ represents the effective conductivity, and σ_{Li} and σ_e represent the conductivities of electrodes and electrolytes respectively.

Mechanical balance equation：

$$\nabla\cdot\left(C_{ijkl}\varepsilon_{kl}^{E}\right)=0$$

$$\varepsilon_{kl}^{E}=\varepsilon_{kl}^{T}-\lambda_i h(\xi)\delta_{ij}$$

$$\varepsilon^{T}=1/2[(\nabla u)^{T}+\nabla u].$$

Where ε_{kl}^{T} is total strain，and λ_i is Vega strain coefficient.

Mode：

This mechano-electrochemical model is available in COMSOL Multiphysics 6.2.This work established a two-dimensional model with a size of 50 × 50 μm. Use the smallest triangular mesh to discretize the simulation domain by 50nm, with a maximum size of 1 μm. Adaptive mesh refinement can improve convergence and accuracy. Set the upper and lower boundaries to 0.10V for voltage. For the 2D model, a plane strain assumption was proposed. The detailed setting of boundary conditions is shown in **Fig. S51**. And the above parameters are detailed in **Table S1**.

2. List of Supporting Figures and Tables

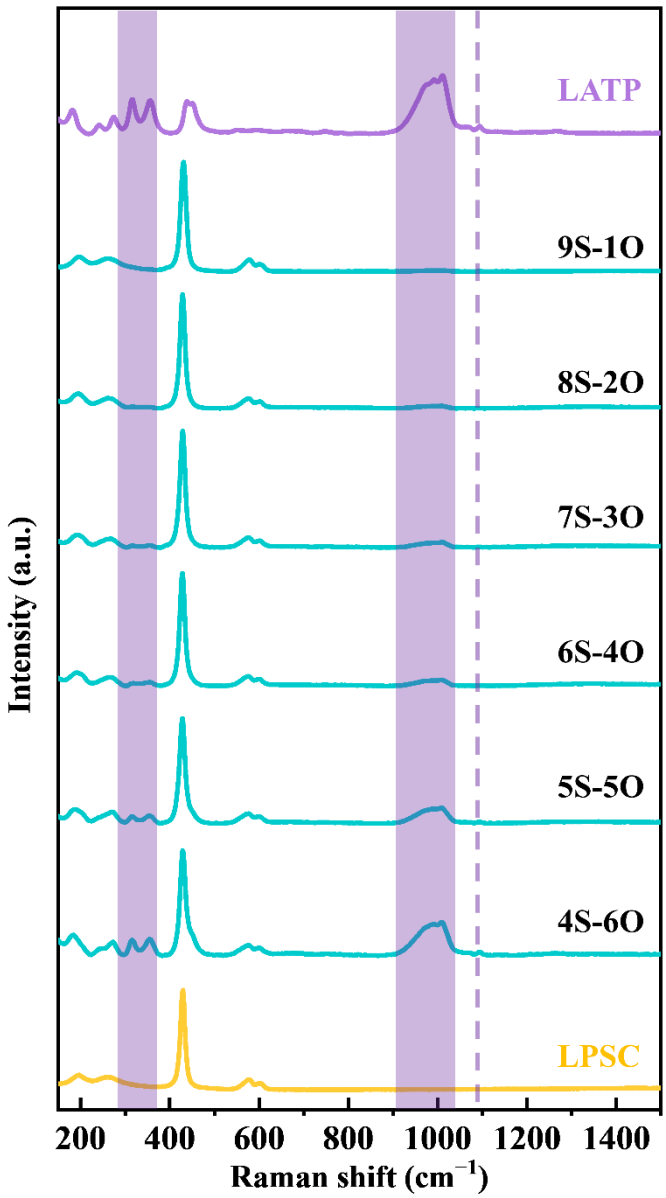

Fig. S1 Raman spectra of 9S-1O, 8S-2O, 7S-3O, 6S-4O, 5S-5O and 4S-6O composite electrolytes with pure LPSC and LATP as references.

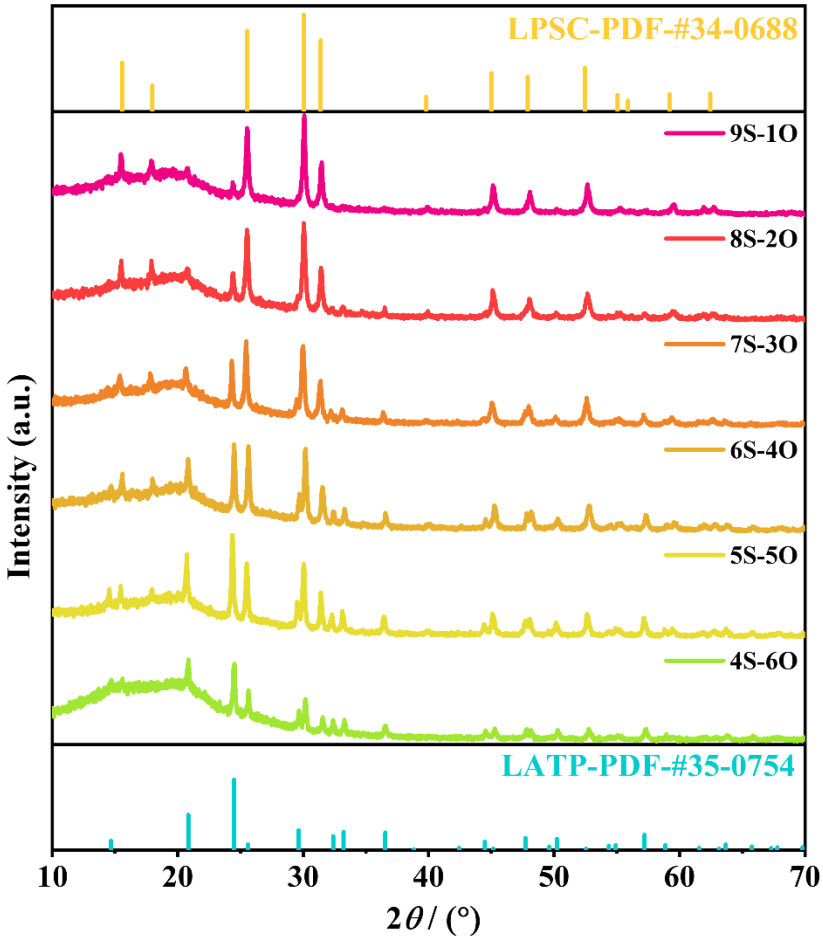

Fig. S2 XRD patterns of 9S-1O, 8S-2O, 7S-3O, 6S-4O, 5S-5O and 4S-6O composite electrolytes, respectively.

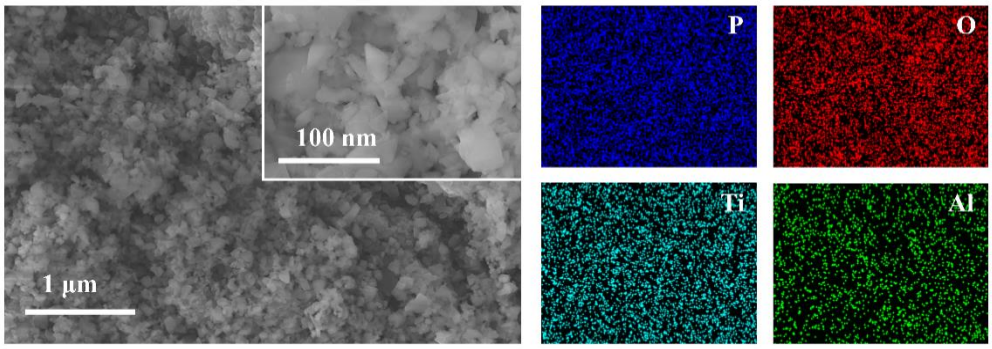

Fig. S3 SEM & EDS observations of LATP powder.

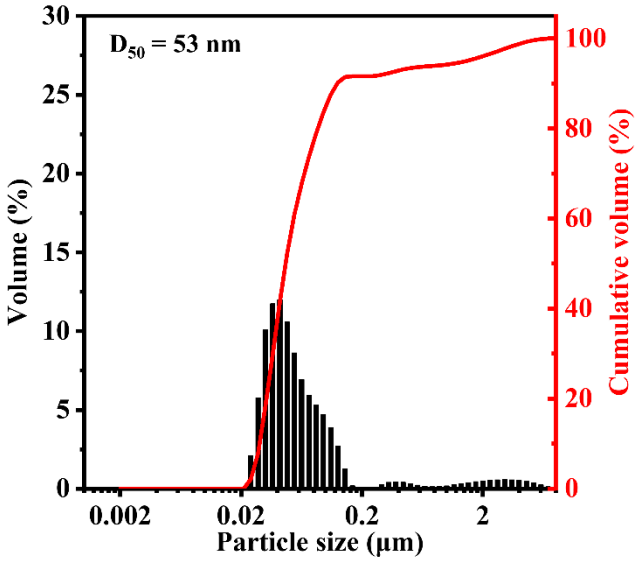

Fig. S4 Particle size distribution of LATP powder.

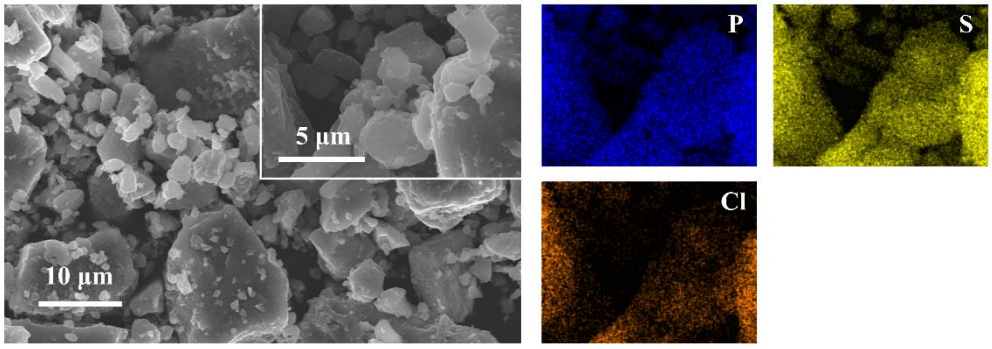

Fig. S5 SEM & EDS observations of LPSC powder.

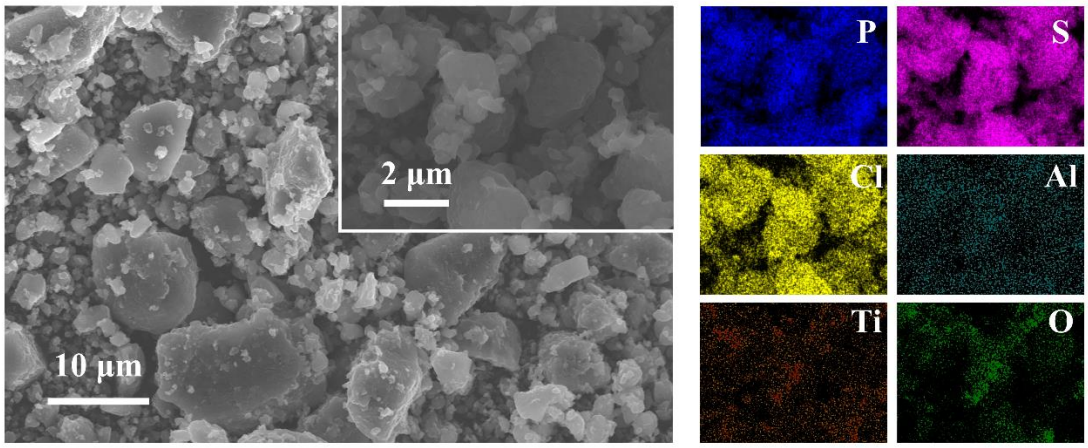

Fig. S6 SEM & EDS observations of 9S-1O composite powder.

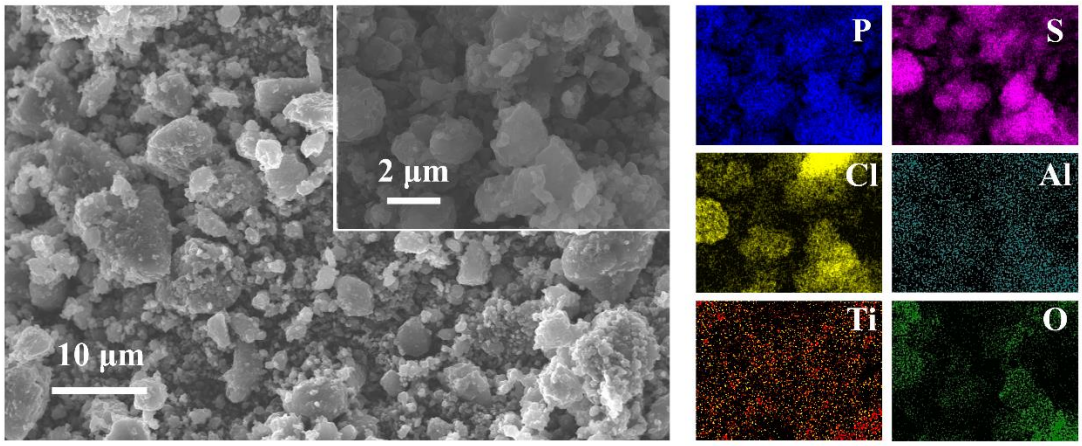

Fig. S7 SEM & EDS observations of 8S-2O composite powder.

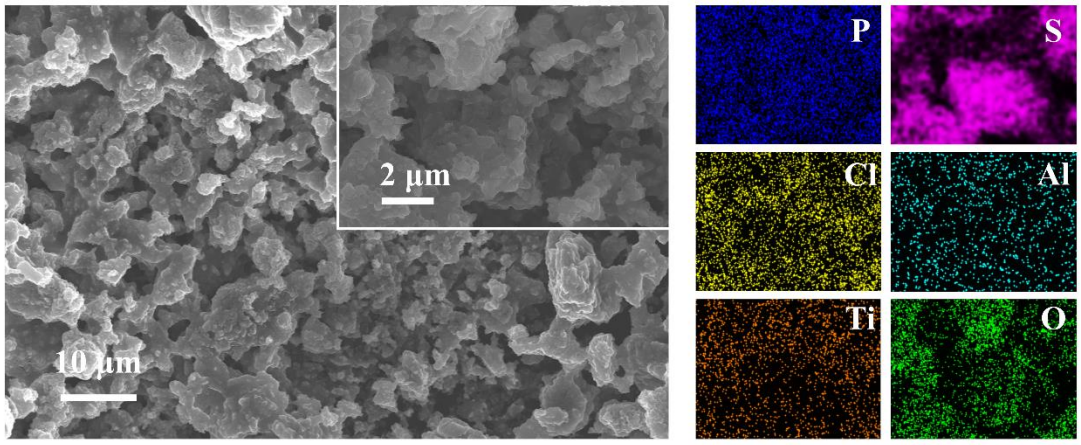

Fig. S8 SEM & EDS observation of 7S-3O composite powder.

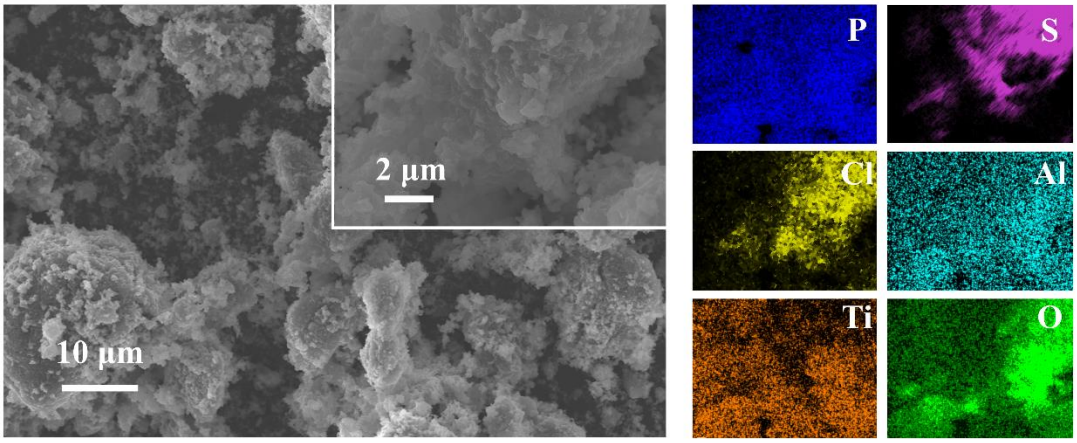

Fig. S9 SEM & EDS observations of 6S-4O composite powder.

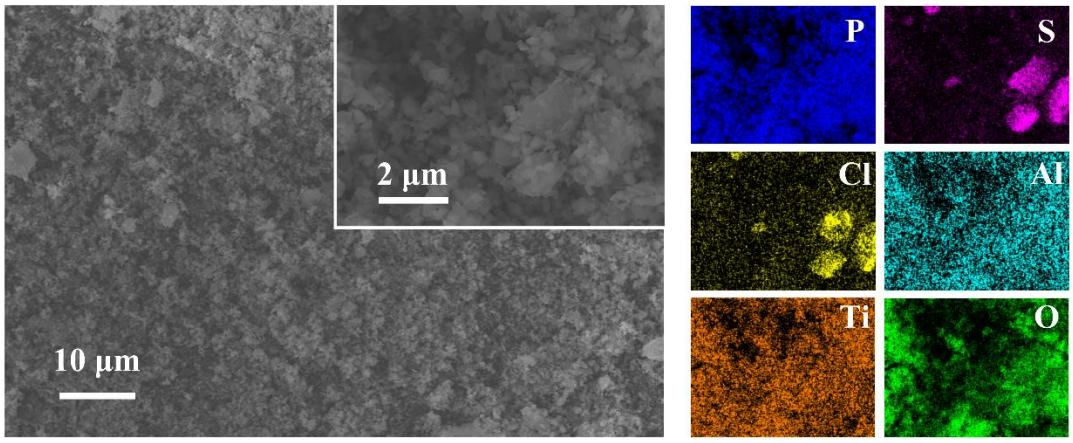

Fig. S10 SEM & EDS observation of 5S-5O composite powder.

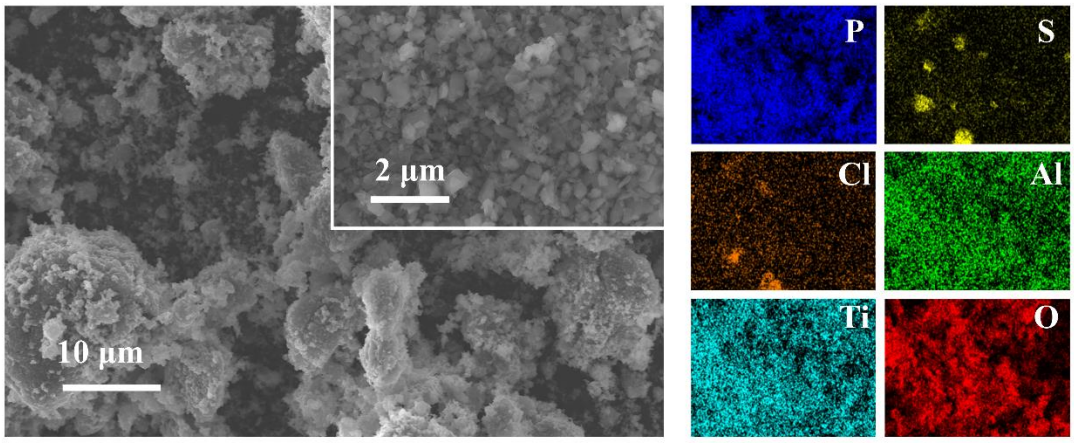

Fig. S11 SEM & EDS observation of 4S-6O composite powder.

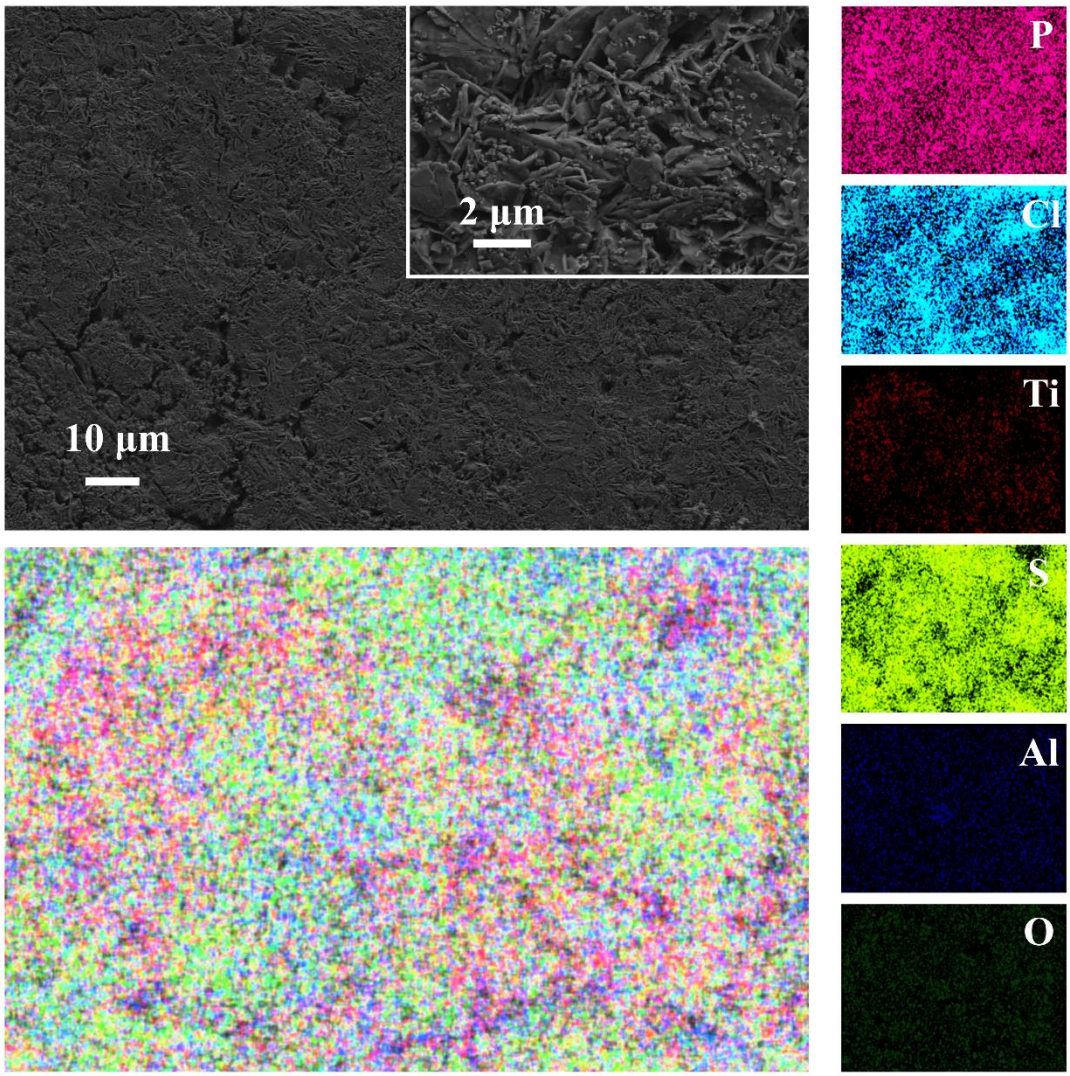

Fig. S12 SEM & EDS observations of surface of 9S-1O composite electrolyte pellet.

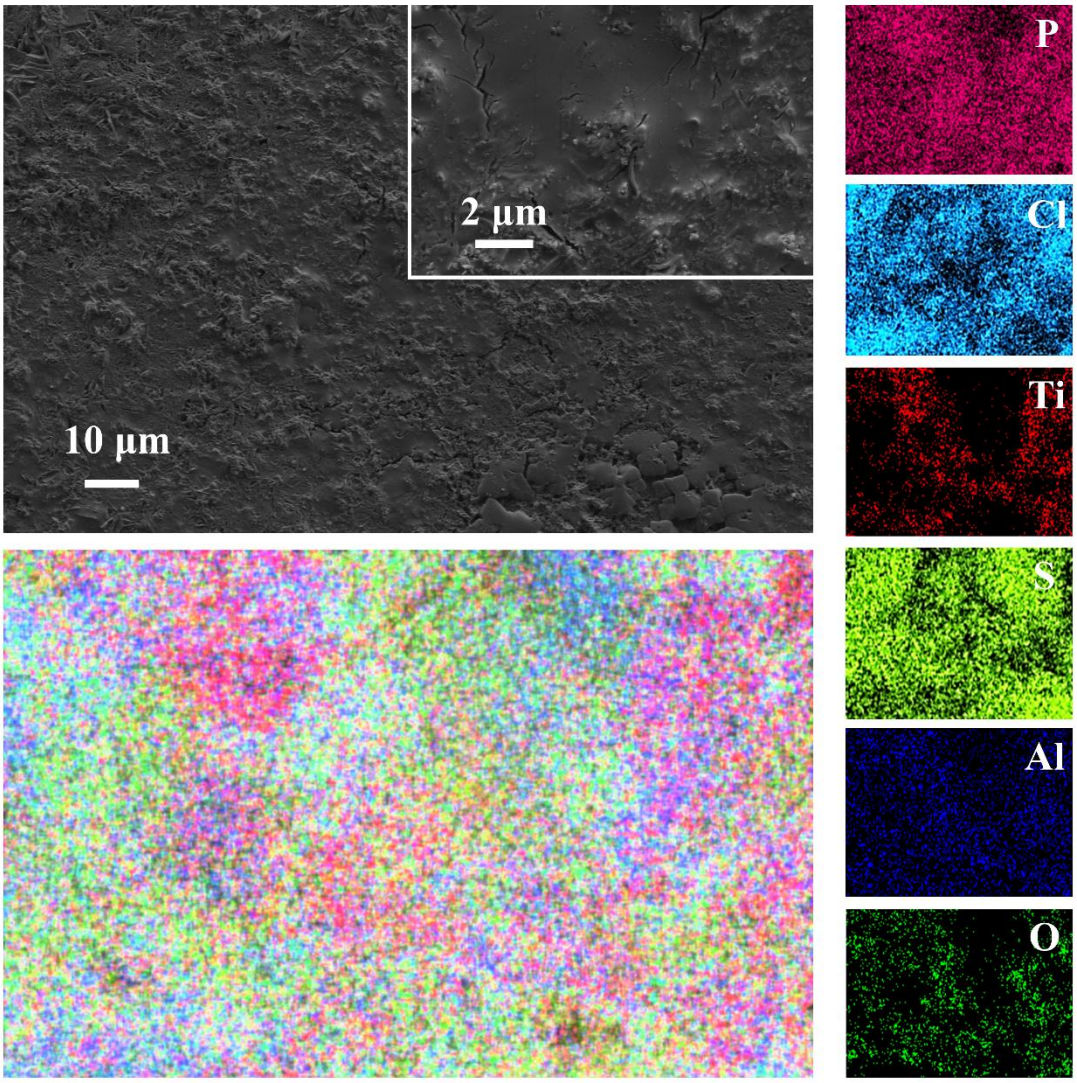

Fig. S13 SEM & EDS observations of surface of 8S-2O composite electrolyte pellet.

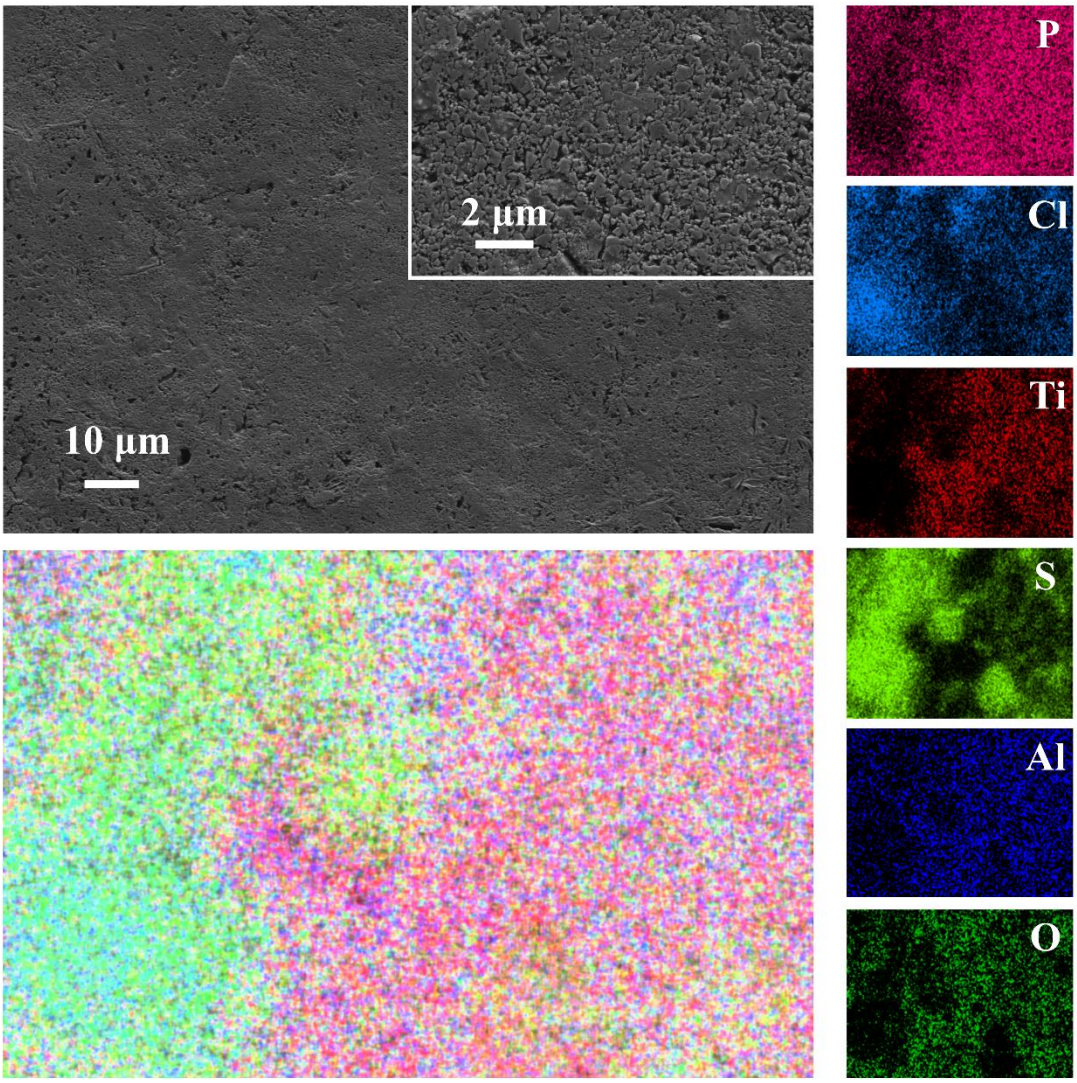

Fig. S14 SEM & EDS observations of surface of 7S-3O composite electrolyte pellet.

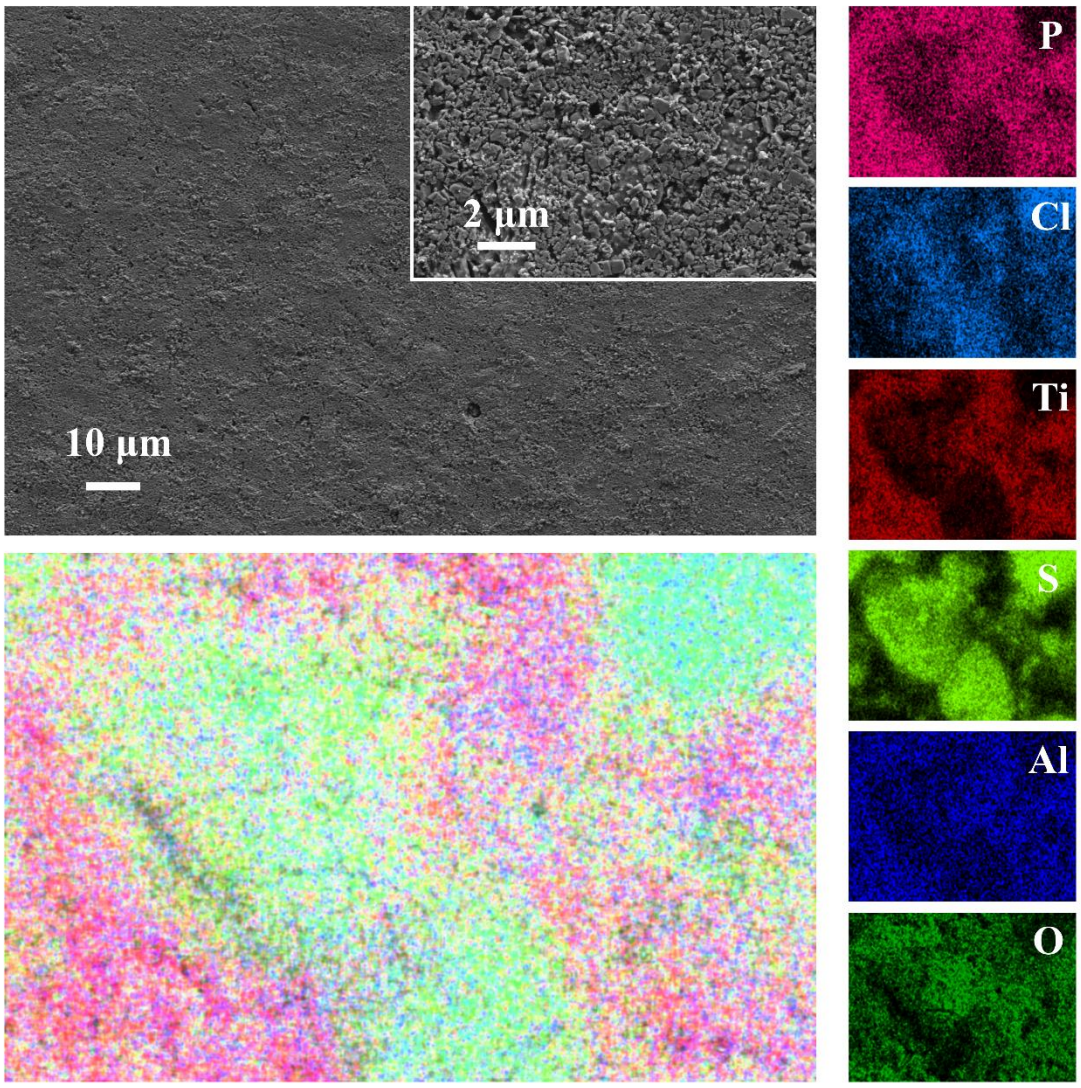

Fig. S15 SEM & EDS observations of surface of 6S-4O composite electrolyte pellet.

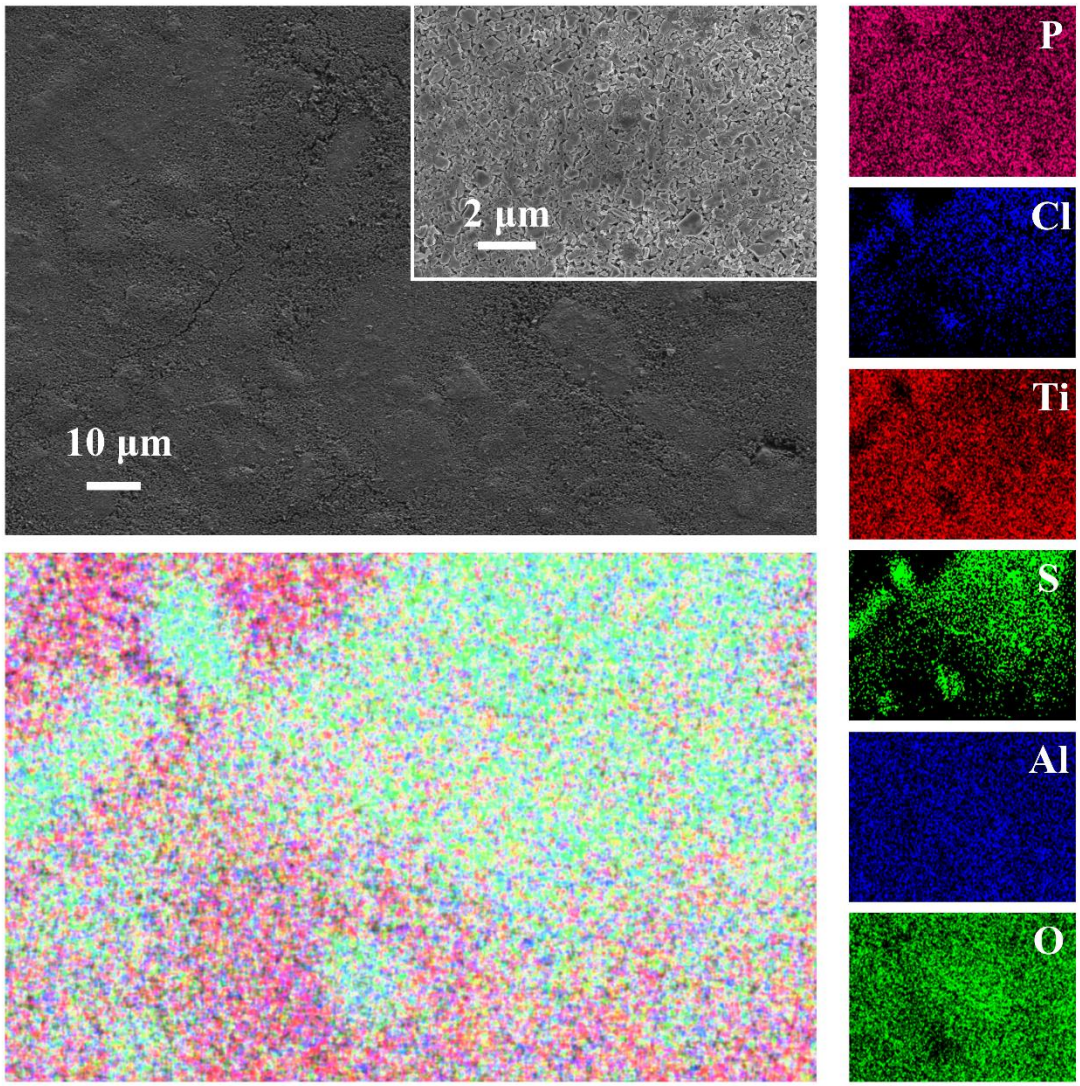

Fig. S16 SEM & EDS observations of surface of 5S-5O composite electrolyte pellet.

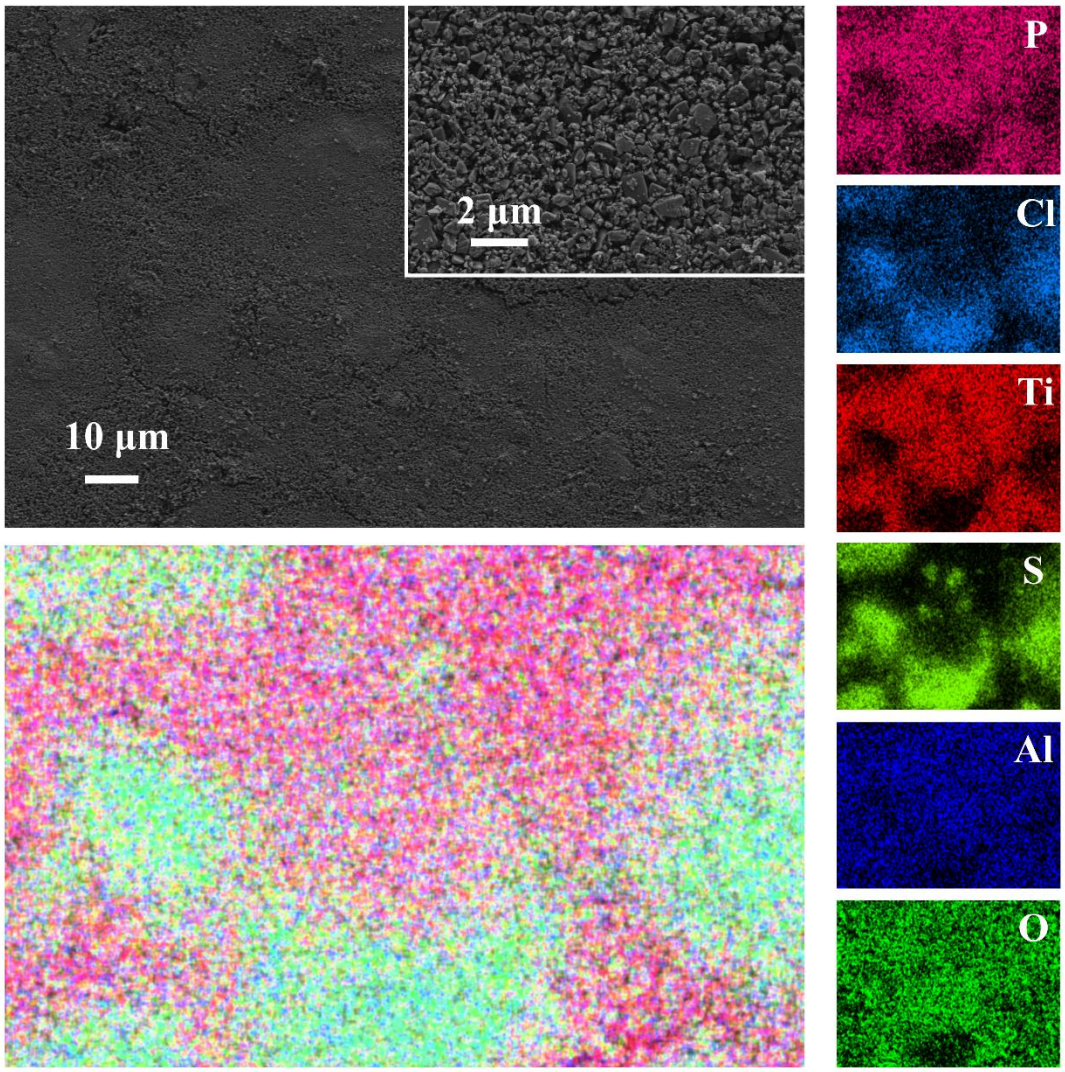

Fig. S17 SEM & EDS observations of surface of 4S-6O composite electrolyte pellet.

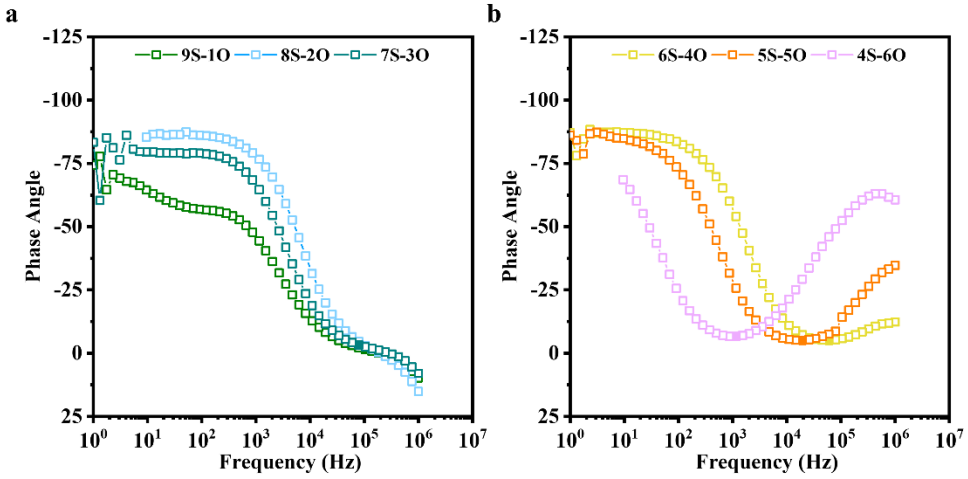

Fig. S18 Bode plots of (a) 9S-1O, 8S-2O, 7S-3O electrolytes and (b) 6S-4O, 5S-5O, 4S-6O electrolytes.

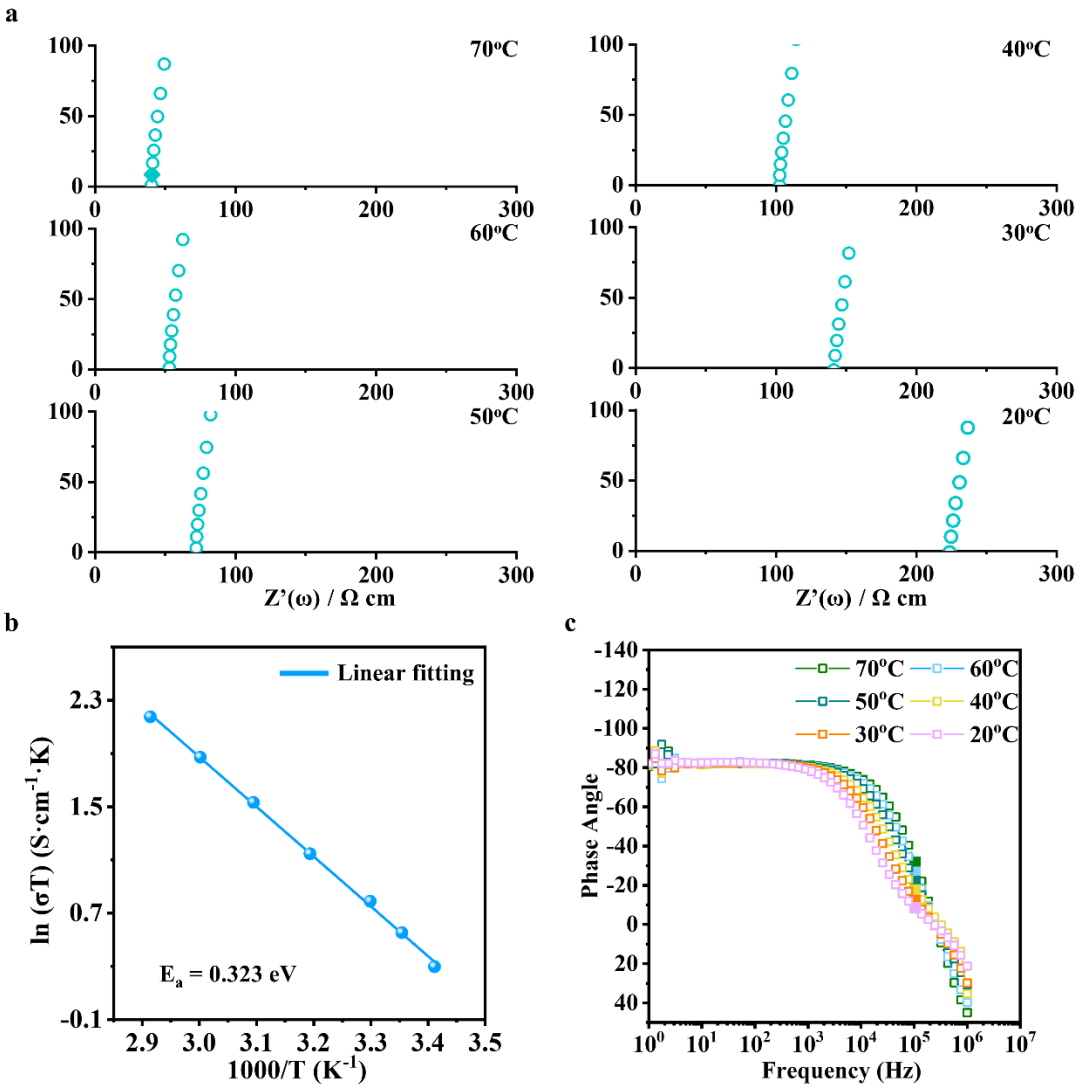

Fig. S19 (a) EIS profiles and (c) Bode plots of LPSC electrolyte at different temperatures. (b) Arrhenius plot of LPSC electrolyte.

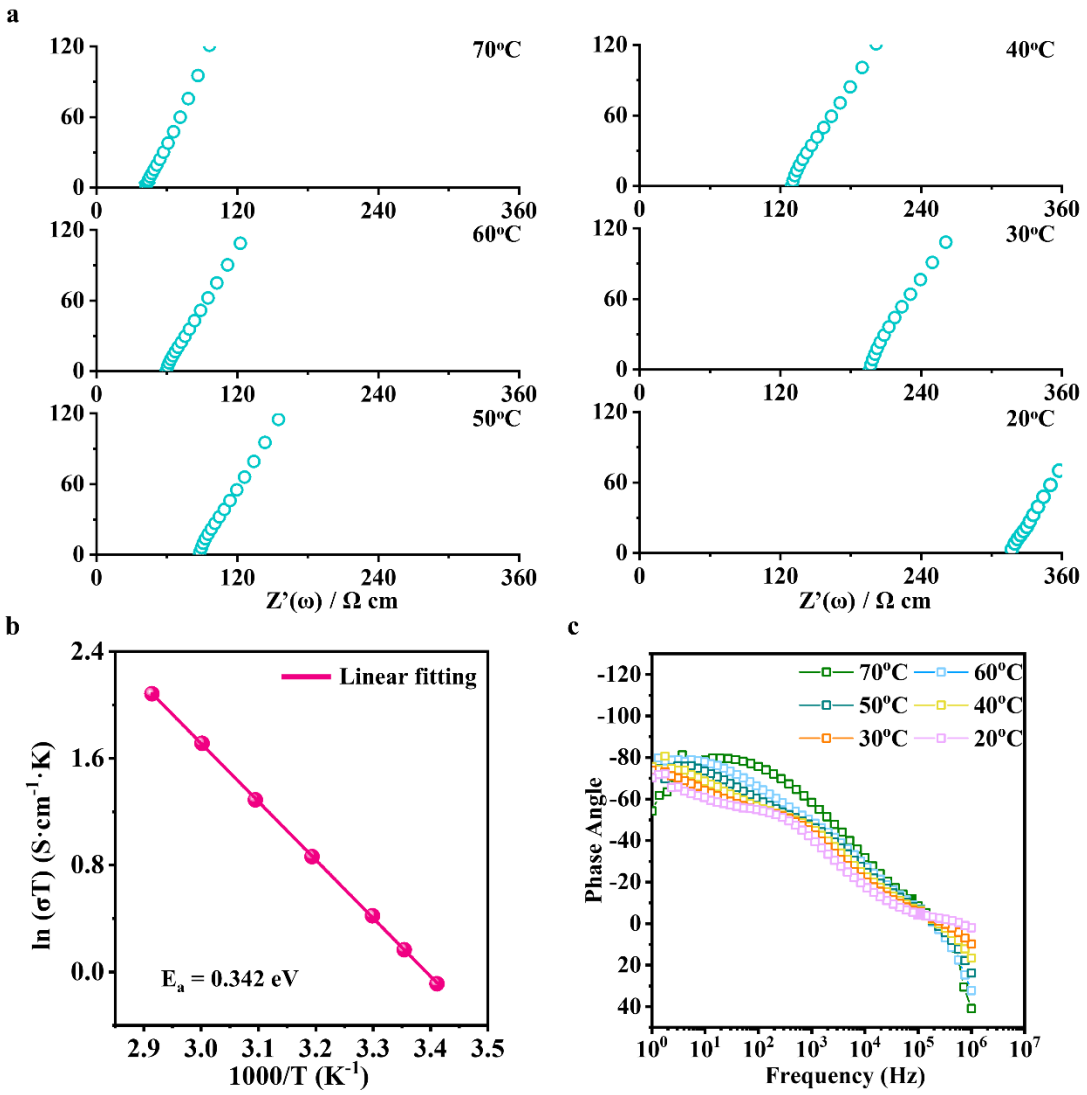

Fig. S20 (a) EIS profiles and (c) Bode plots of 9S-1O composite electrolyte at different temperatures. (b) Arrhenius plot of 9S-1O composite electrolyte.

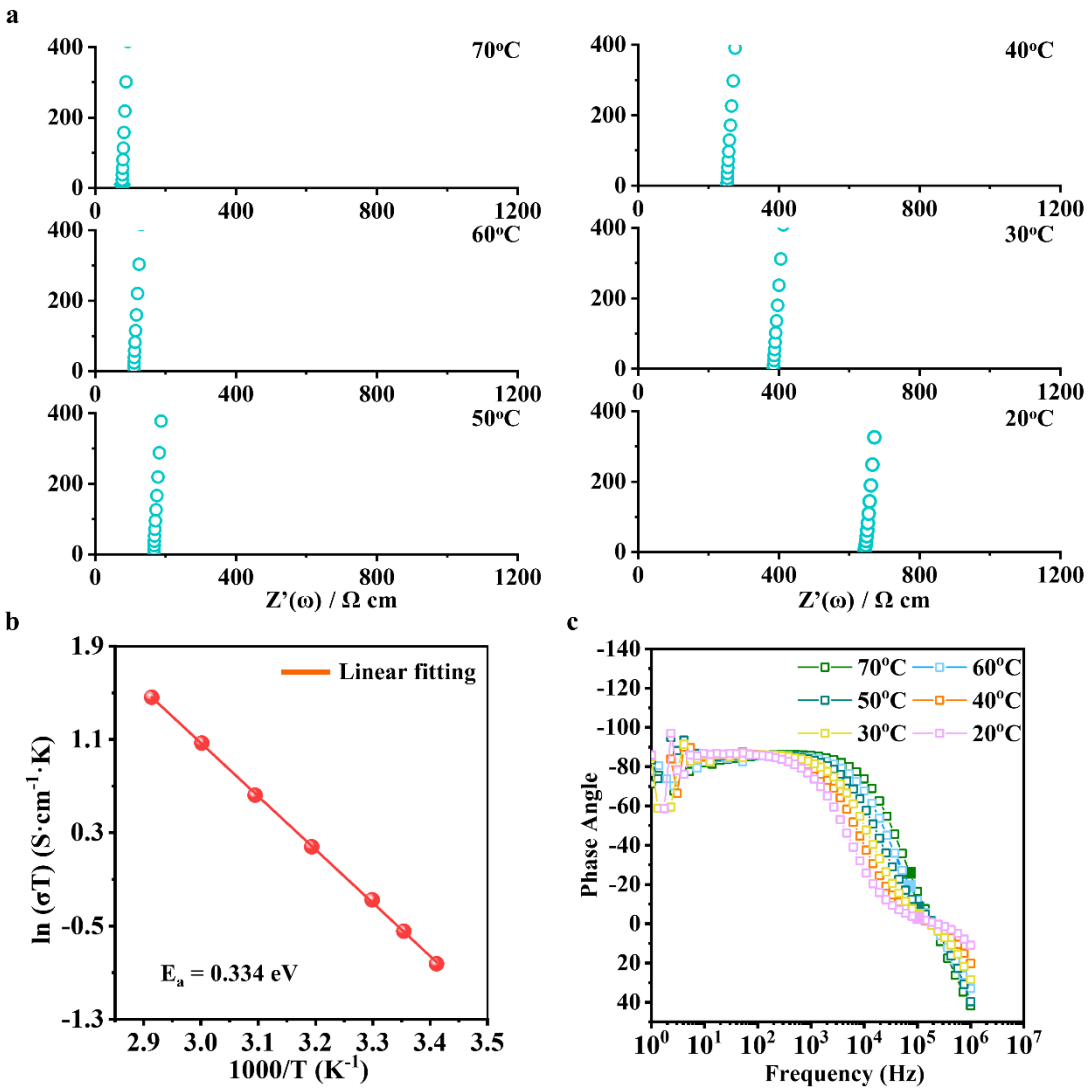

Fig. S21 (a) EIS profiles and (c) Bode plots of 8S-2O composite electrolyte at different temperatures. (b) Arrhenius plot of 8S-2O composite electrolyte.

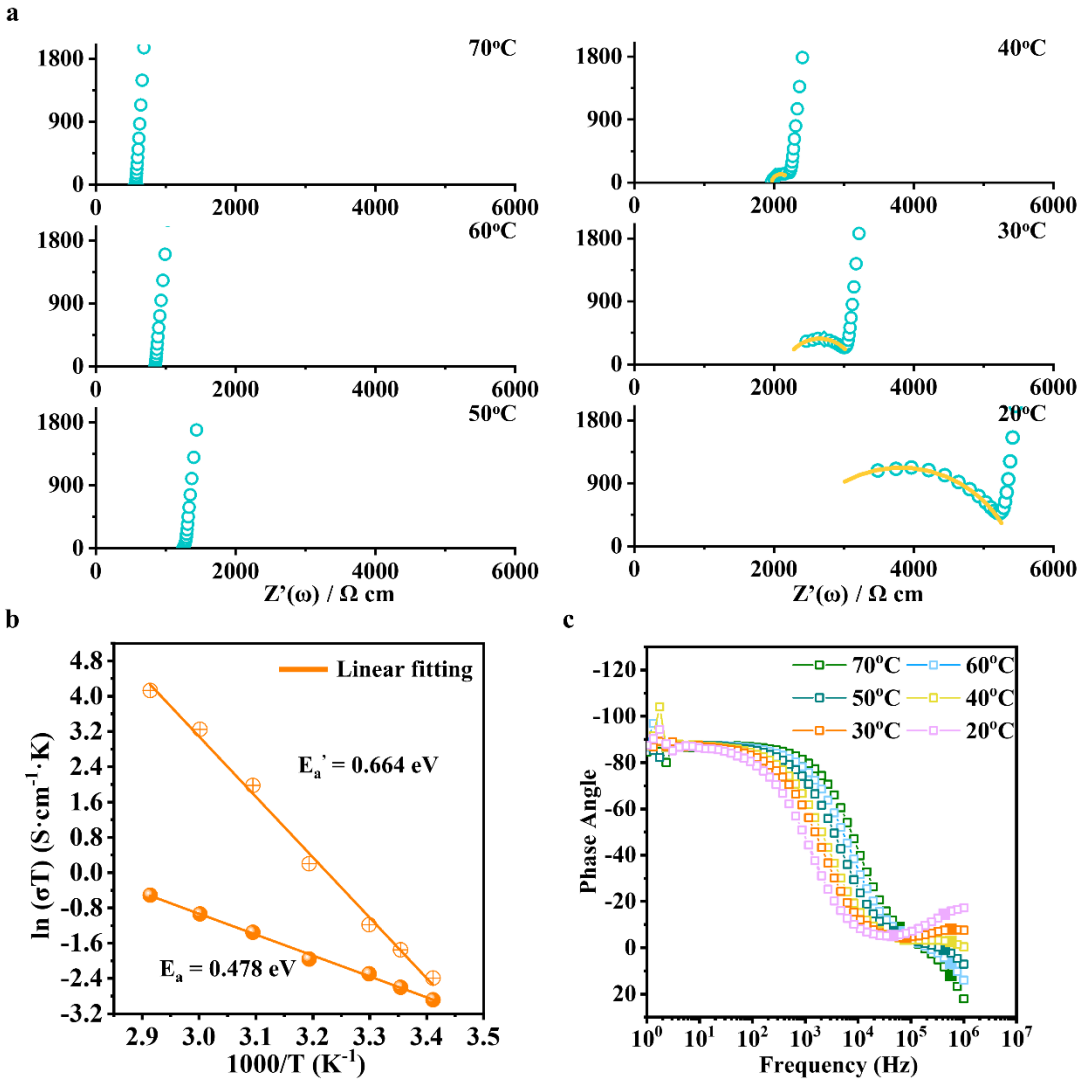

Fig. S22 (a) EIS profiles and (c) Bode plots of 7S-3O composite electrolyte at different temperatures. (b) Arrhenius plot of 7S-3O composite electrolyte.

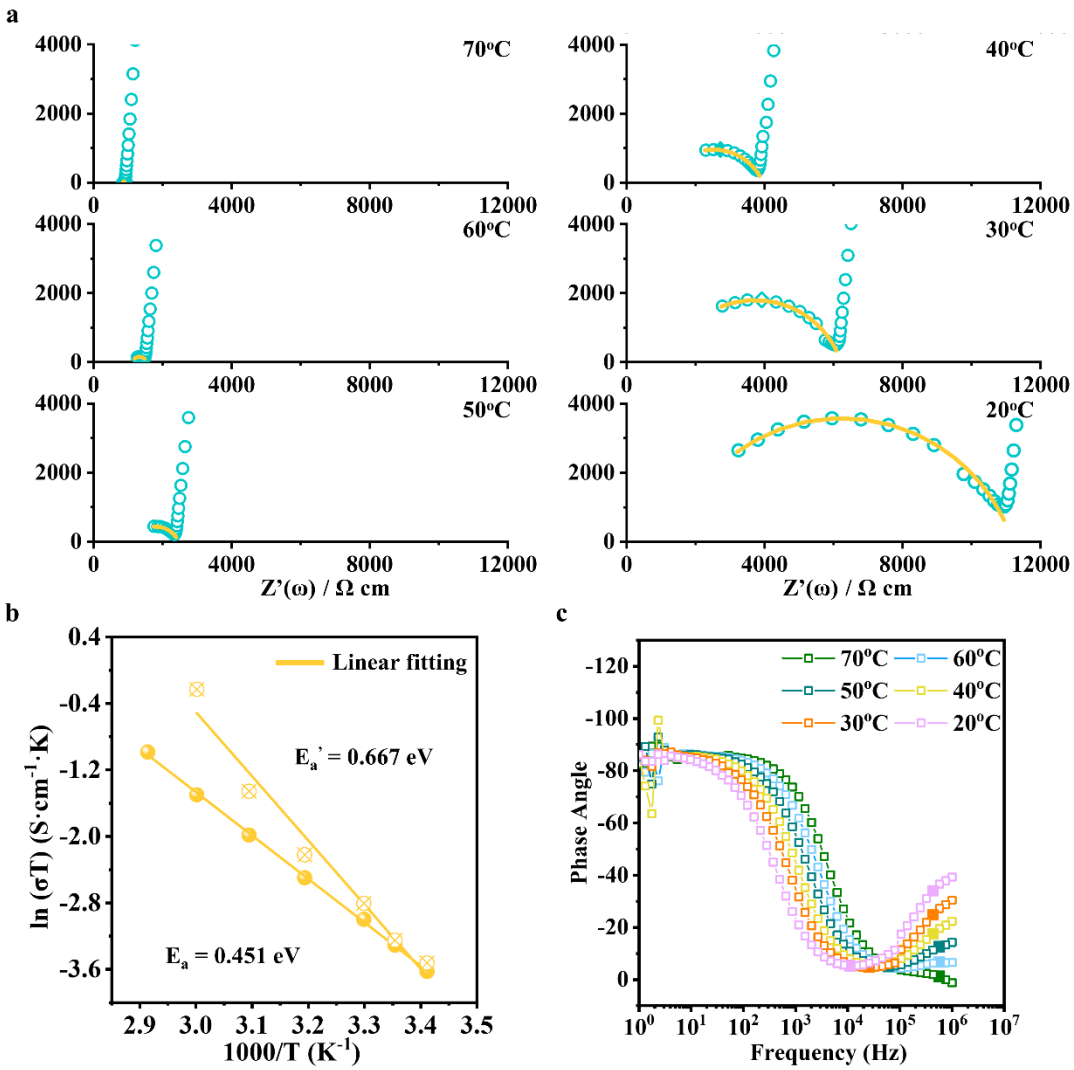

Fig. S23 (a) EIS profiles and (c) Bode plots of 6S-4O composite electrolyte at different temperatures. (b) Arrhenius plot of 6S-4O composite electrolyte.

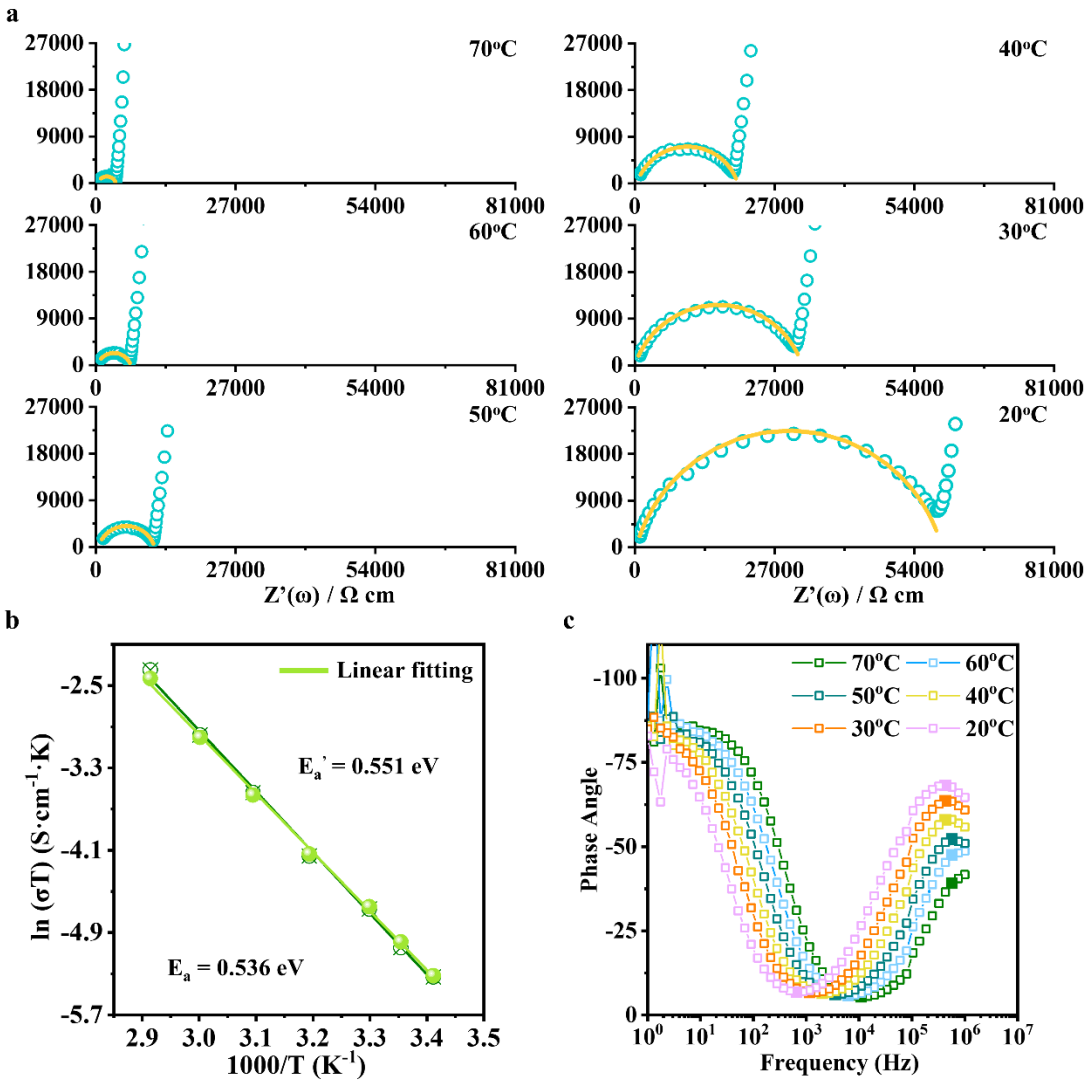

Fig. S24 (a) EIS profiles and (c) Bode plots of 5S-5O composite electrolyte at different temperatures. (b) Arrhenius plot of 5S-5O composite electrolyte.

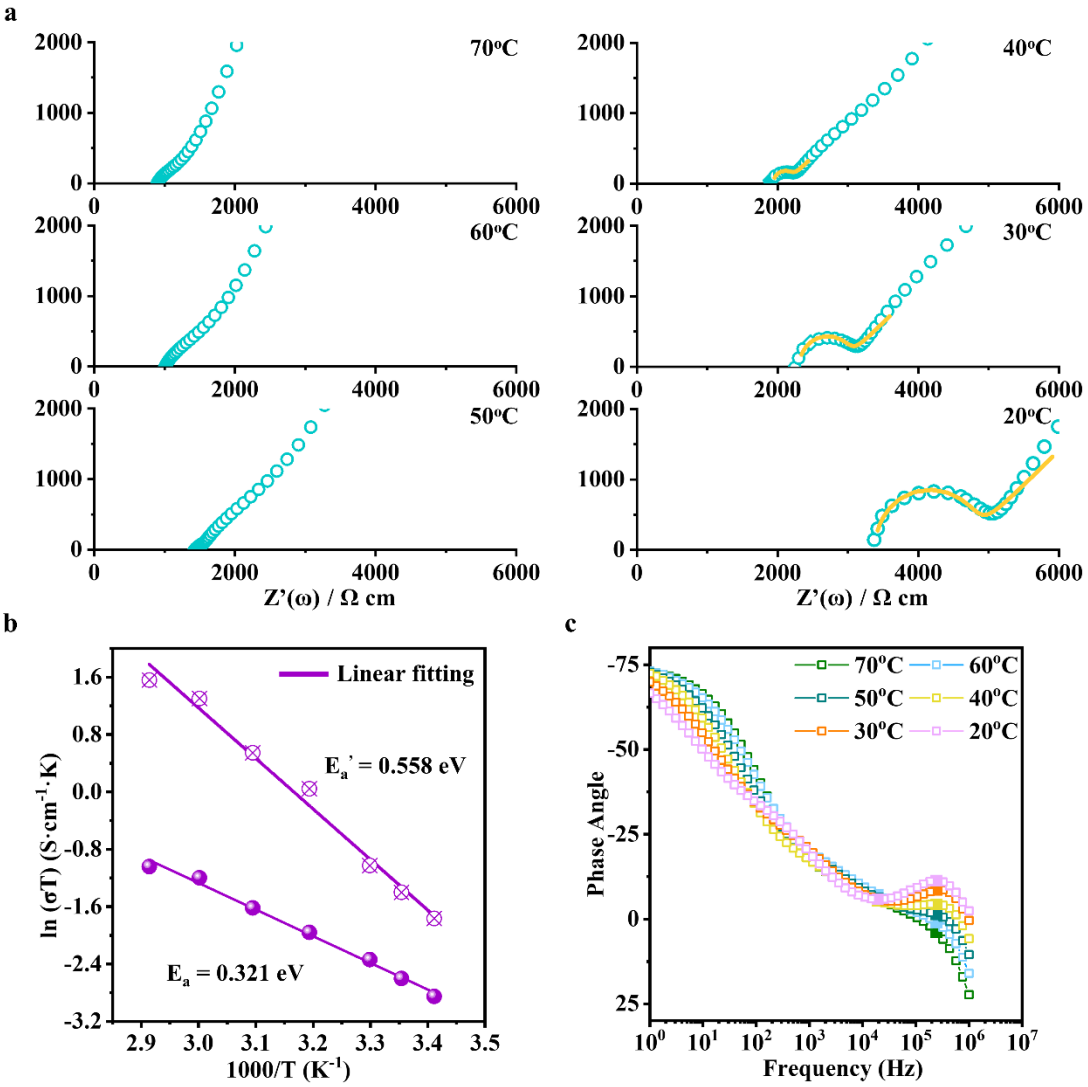

Fig. S25 (a) EIS profiles and (c) Bode plots of LATP electrolyte at different temperatures. (b) Arrhenius plot of LATP electrolyte.

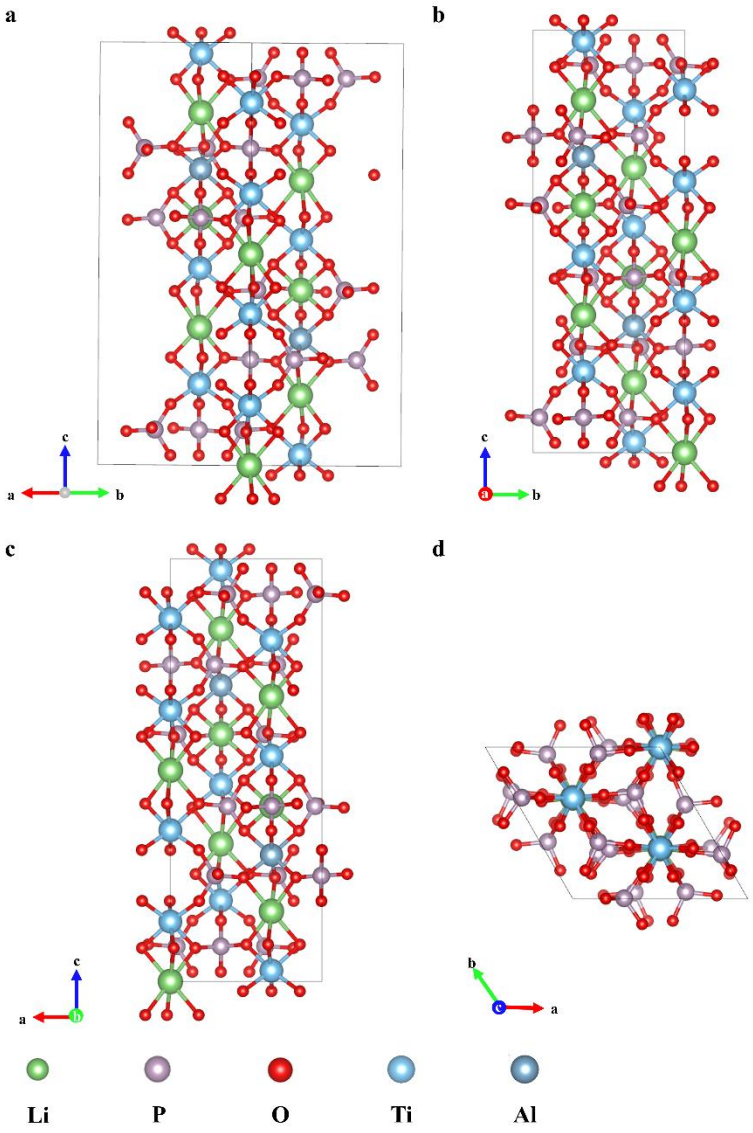

Fig. S26 (a) Crystal structure of LATP accompanied with views along (b) a axis, (c) b axis and (d) c axis.

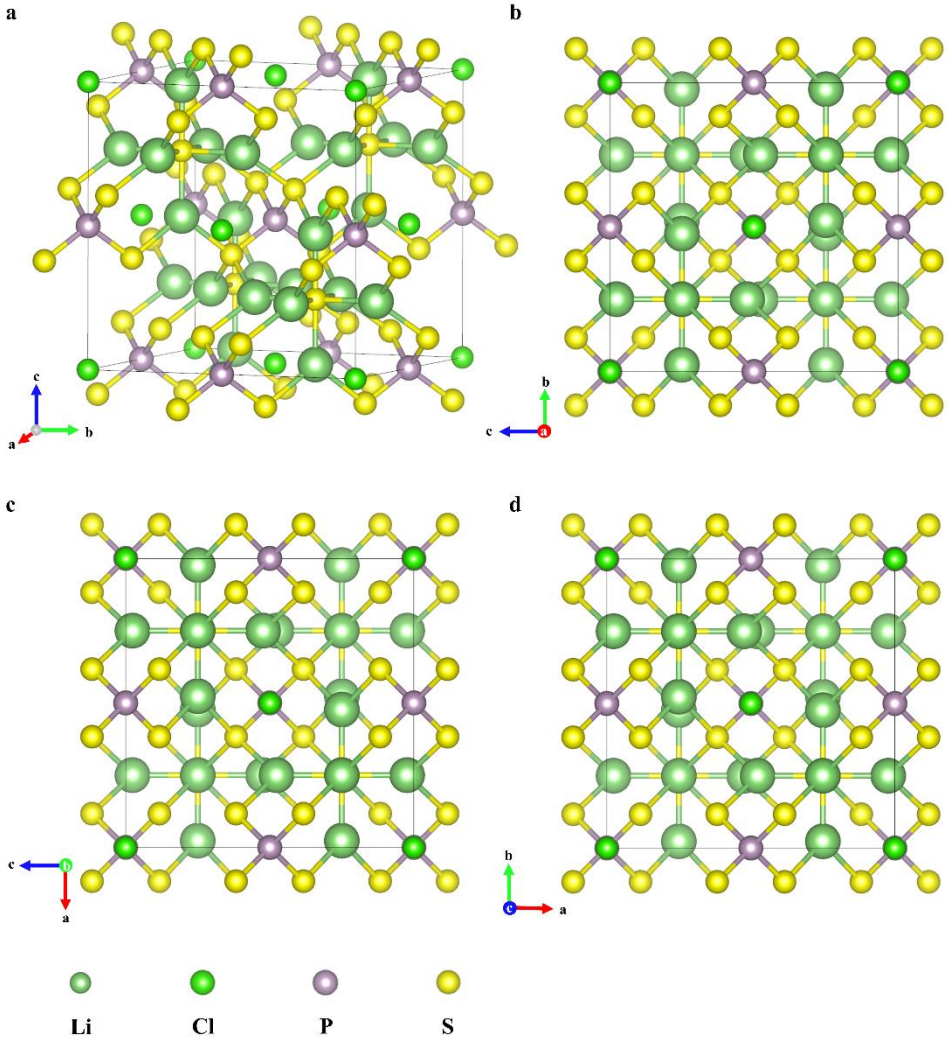

Fig. S27 (a) Crystal structure of LPSC accompanied with views along (b) a axis, (c) b axis and (d) c axis.

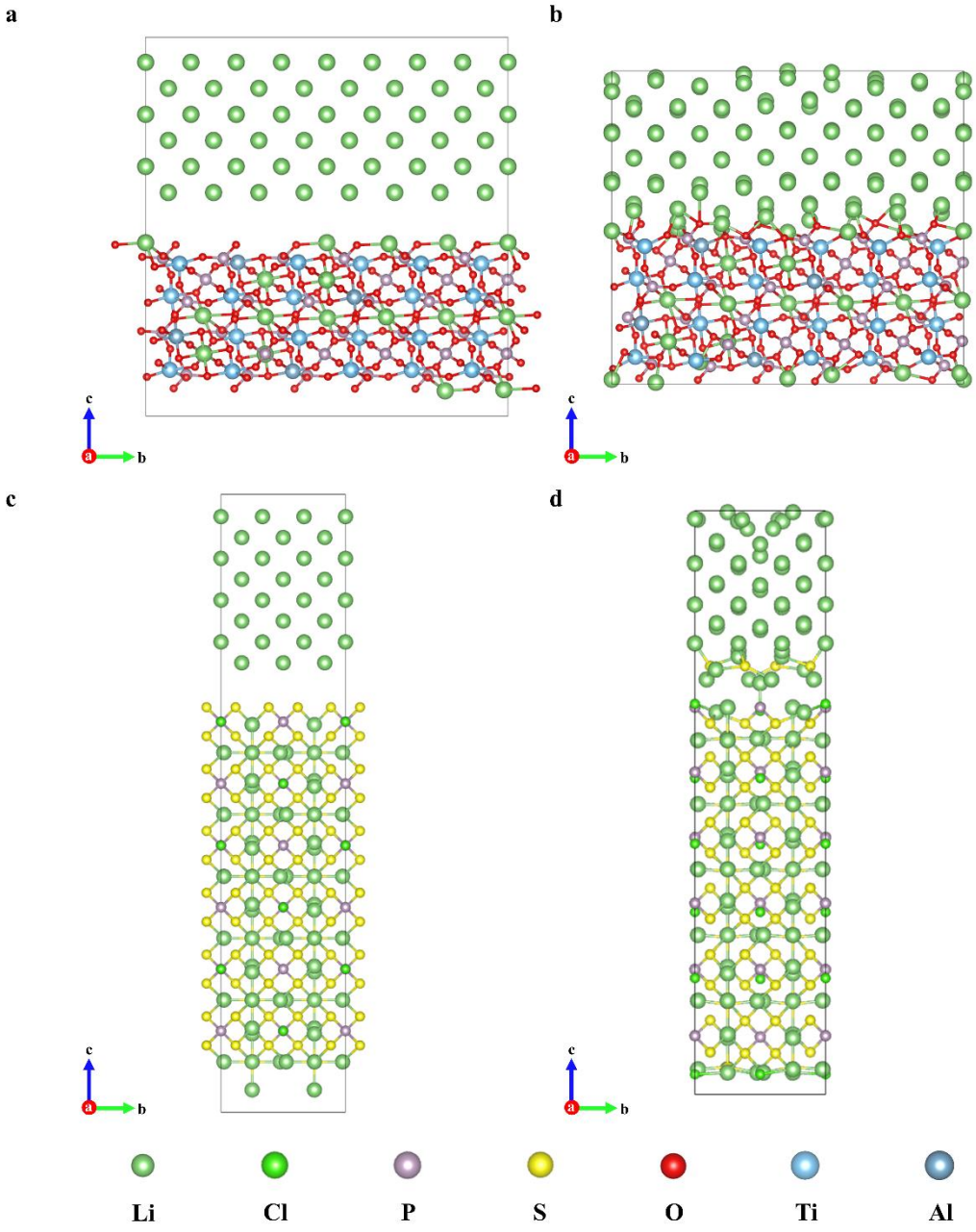

Fig. S28 The simulated crystal structures for Li(001)/LPSC(110) and Li(001)/LATP(012) heterojunction (a-b) before and (c-d) after structural optimizations.

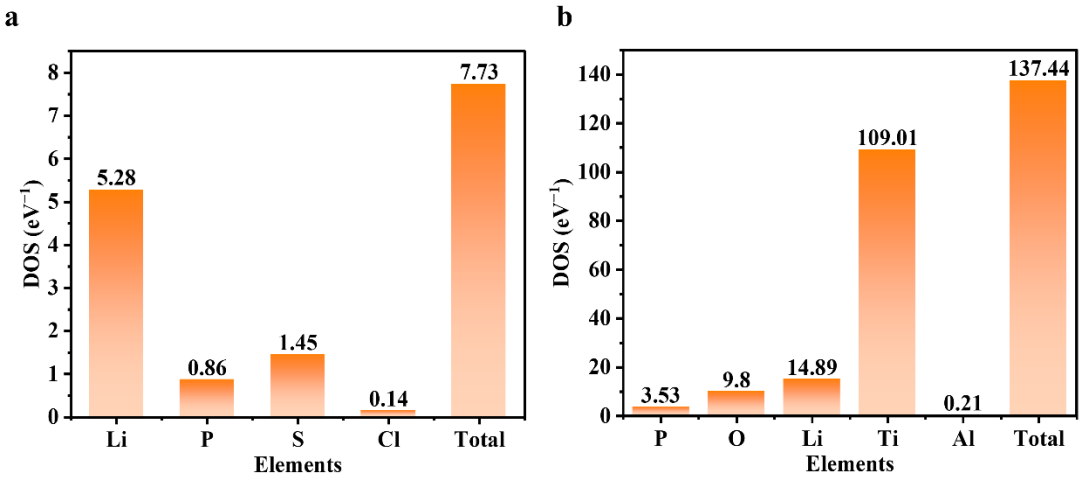

Fig. S29 The DOS at E_f for each element within (a) Li(001)/Li_6PS_5Cl(100) and (b) Li(001)/$Li_{1.3}Al_{0.3}Ti_{1.7}(PO_4)_3$(012) heterojunctions.

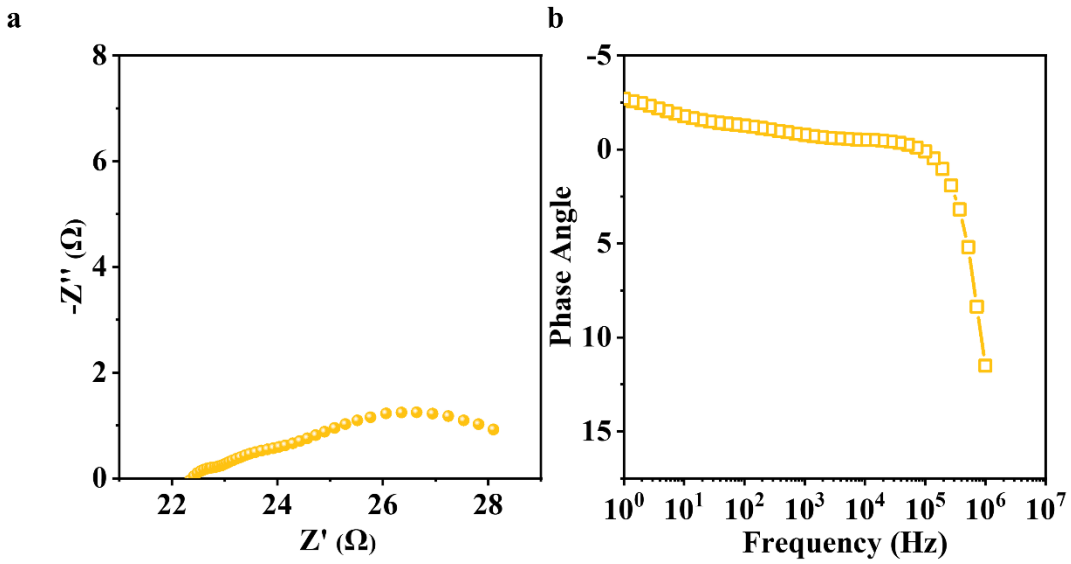

Fig. S30 (a) Nyquist plot and (b) corresponding Bode plot for Li/LPSC/Li symmetric cell.

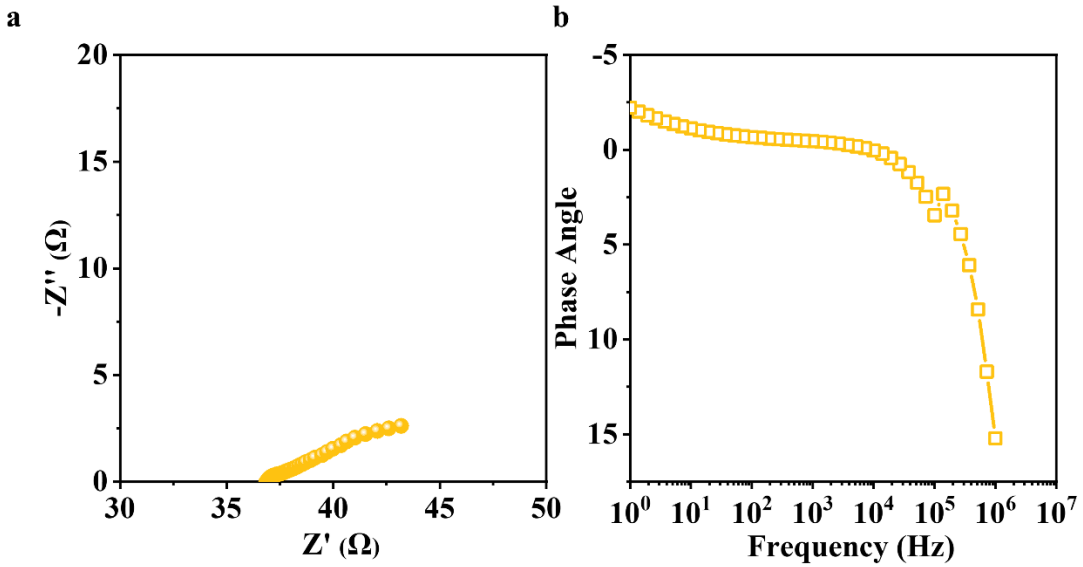

Fig. S31 (a) Nyquist plot and (b) corresponding Bode plot for Li/LPSC/9S-1O/LPSC/Li symmetric cell.

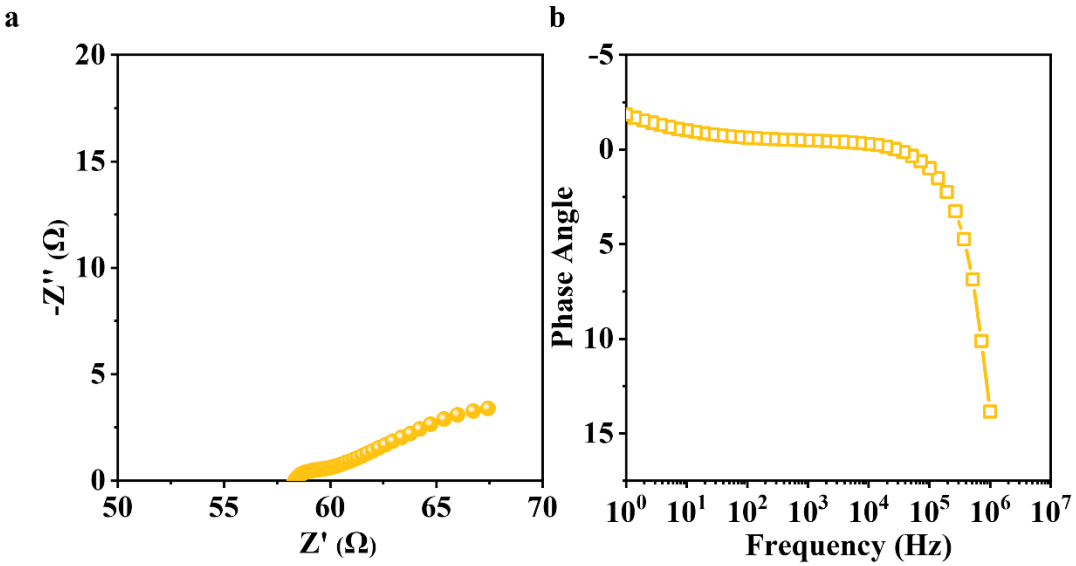

Fig. S32 (a) Nyquist plot and (b) corresponding Bode plot for Li/LPSC/8S-2O/LPSC/Li symmetric cell.

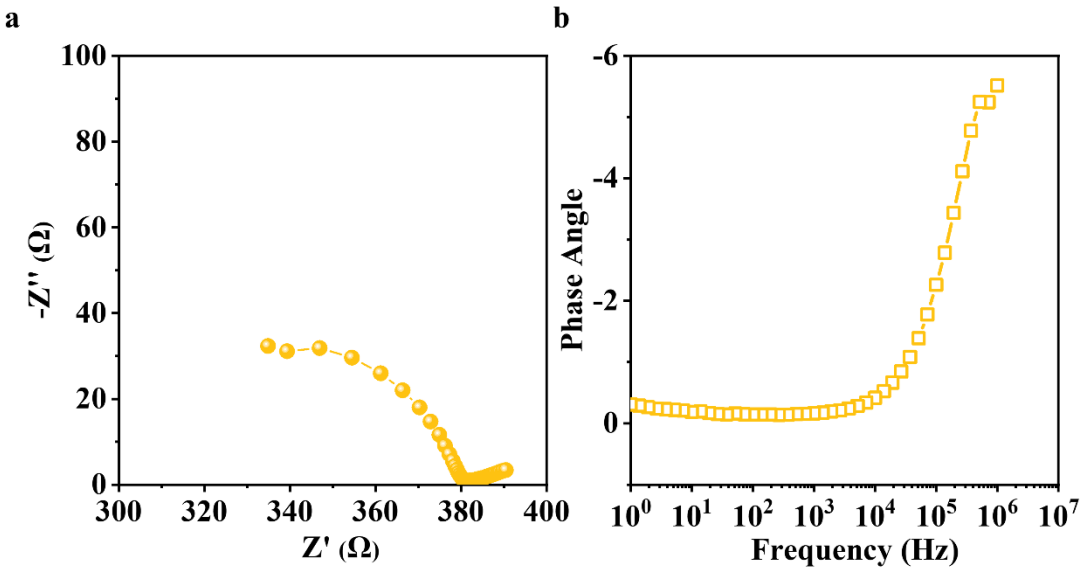

Fig. S33 (a) Nyquist plot and (b) corresponding Bode plot for Li/LPSC/7S-3O/LPSC/Li symmetric cell.

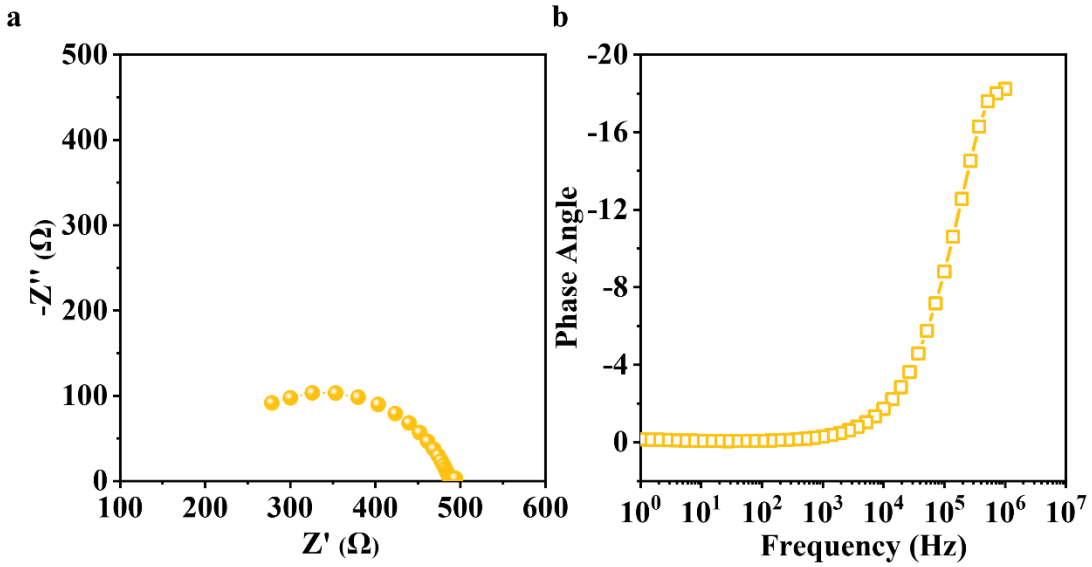

Fig. S34 (a) Nyquist plot and (b) corresponding Bode plot for Li/LPSC/6S-4O/LPSC/Li symmetric cell.

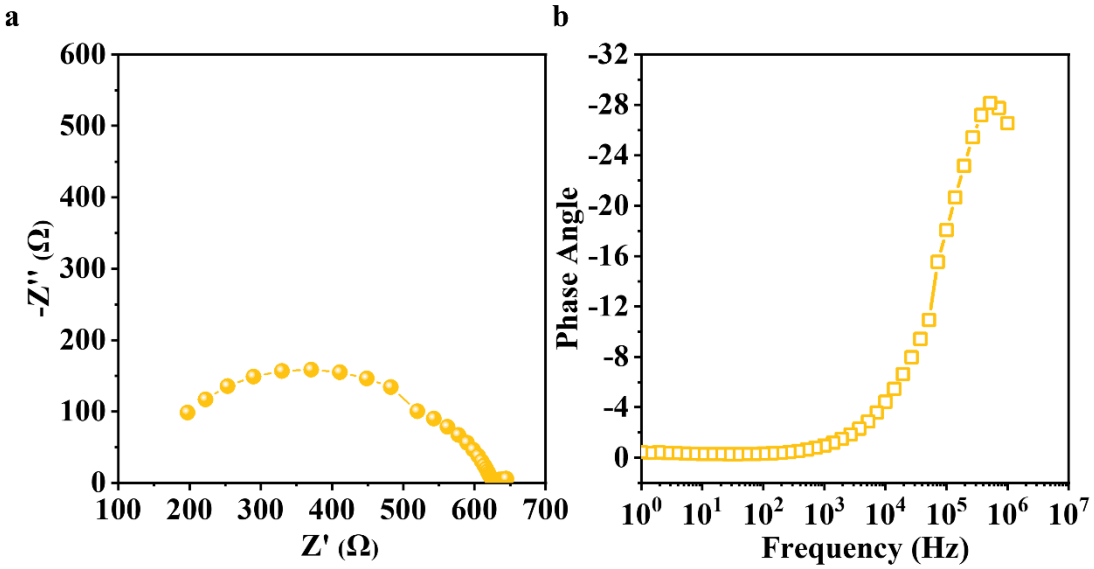

Fig. S35 (a) Nyquist plot and (b) corresponding Bode plot for Li/LPSC/5S-5O/LPSC/Li symmetric cell.

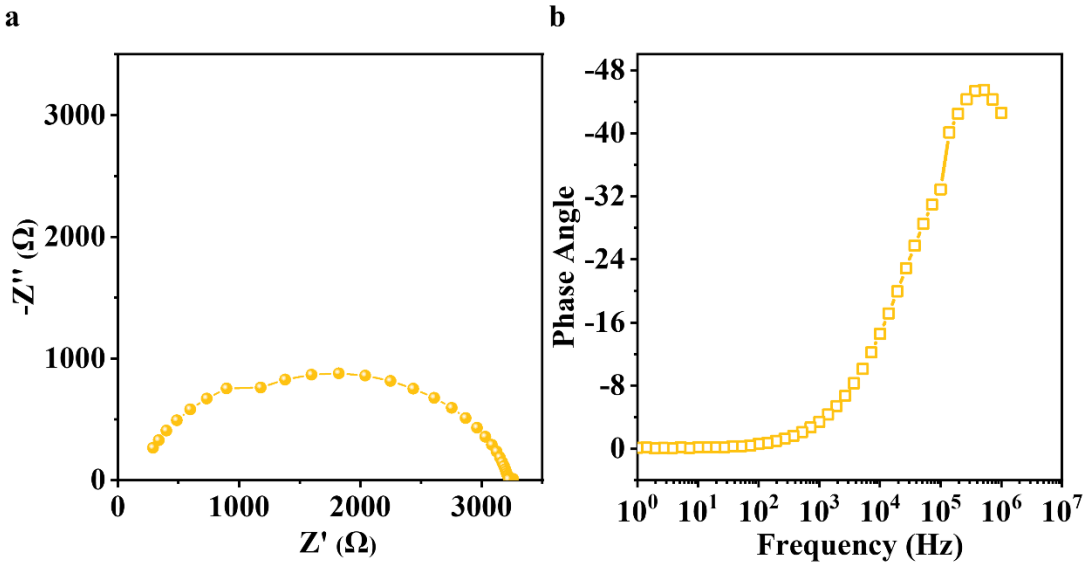

Fig. S36 (a) Nyquist plot and (b) corresponding Bode plot for Li/LPSC/4S-6O/LPSC/Li symmetric cell.

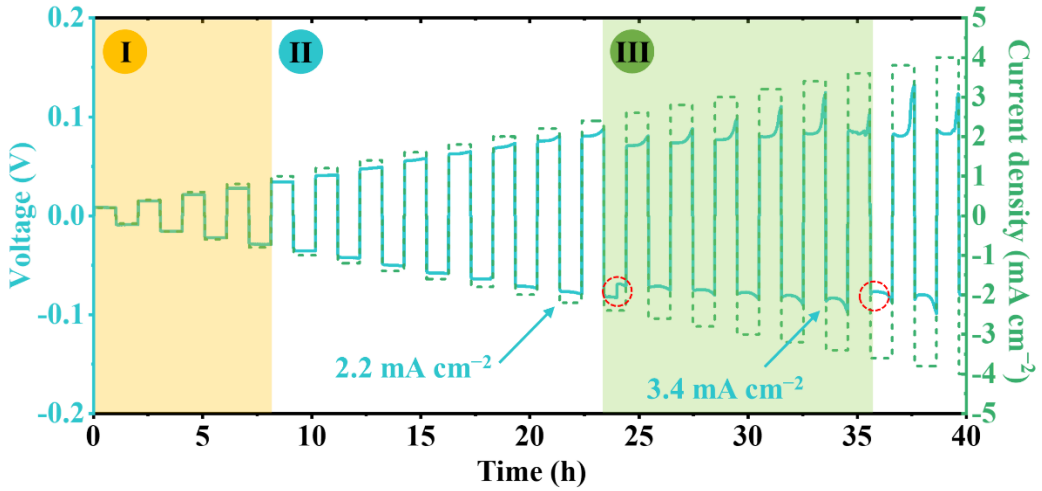

Fig. S37 CCD measurement of Li/LPSC/9S-1O/LPSC/Li symmetric cell.

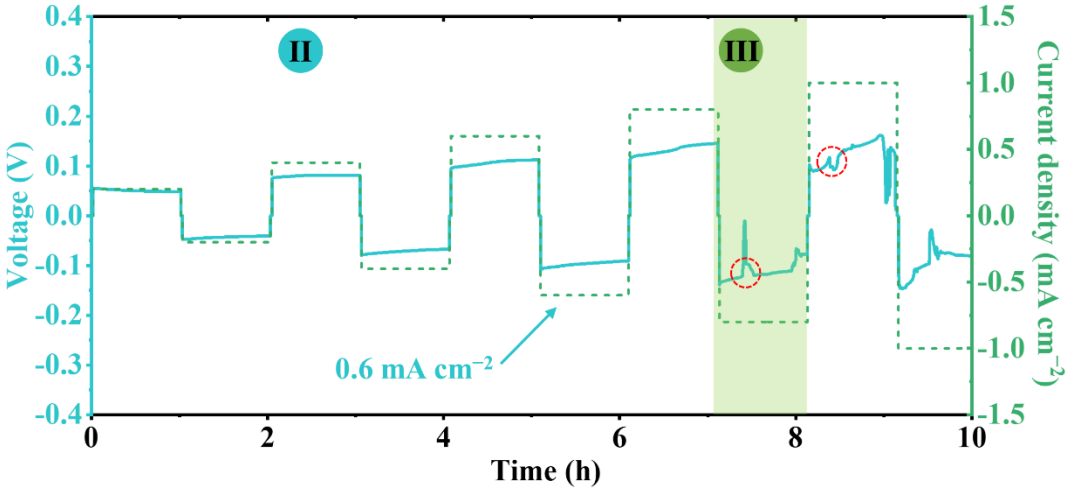

Fig. S38 CCD measurement of Li/LPSC/7S-3O/LPSC/Li symmetric cell.

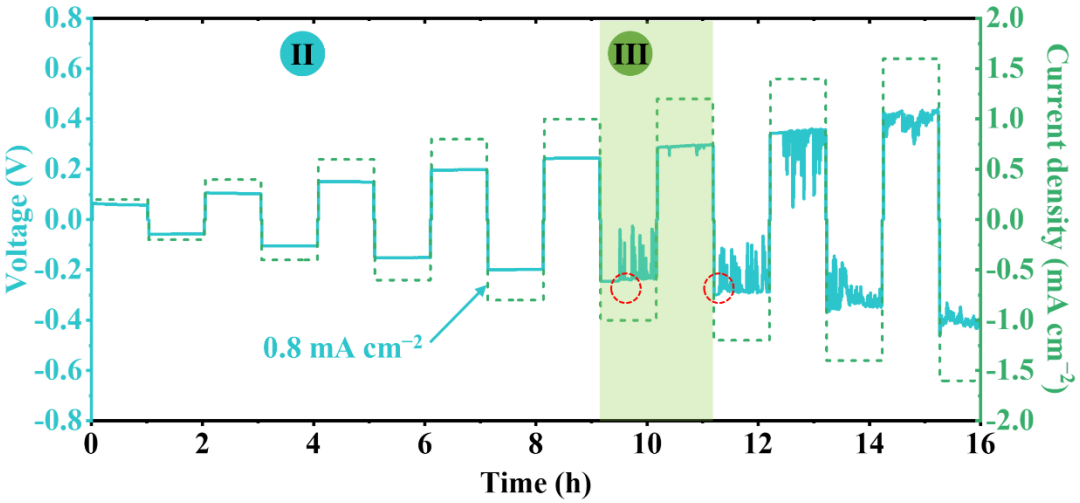

Fig. S39 CCD measurement of Li/LPSC/6S-4O/LPSC/Li symmetric cell.

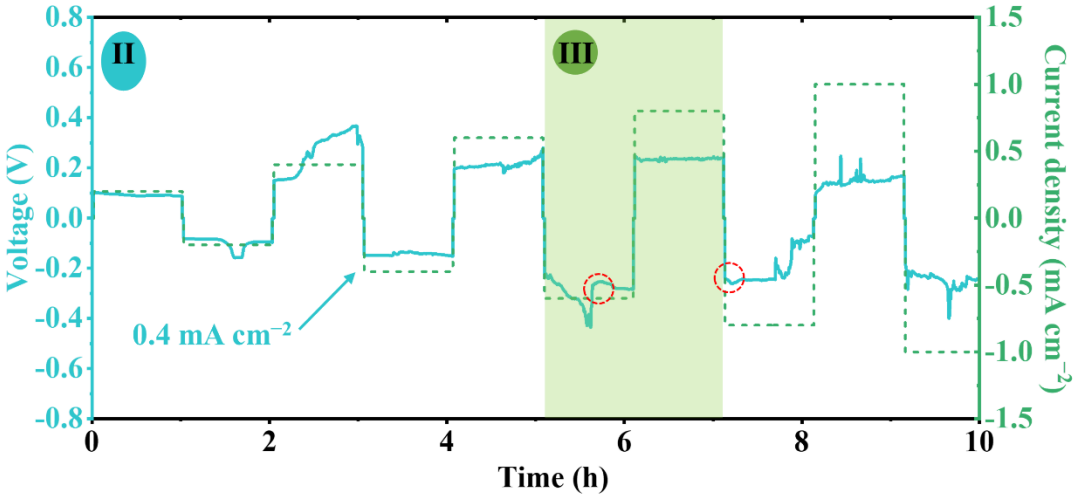

Fig. S40 CCD measurement of Li/LPSC/5S-5O/LPSC/Li symmetric cell.

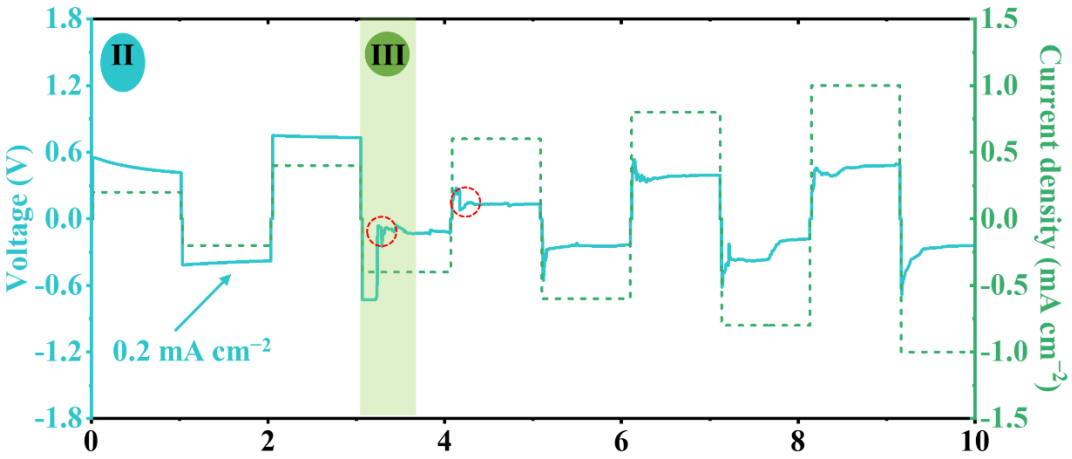

Fig. S41 CCD measurement of Li/LPSC/4S-6O/LPSC/Li symmetric cell.

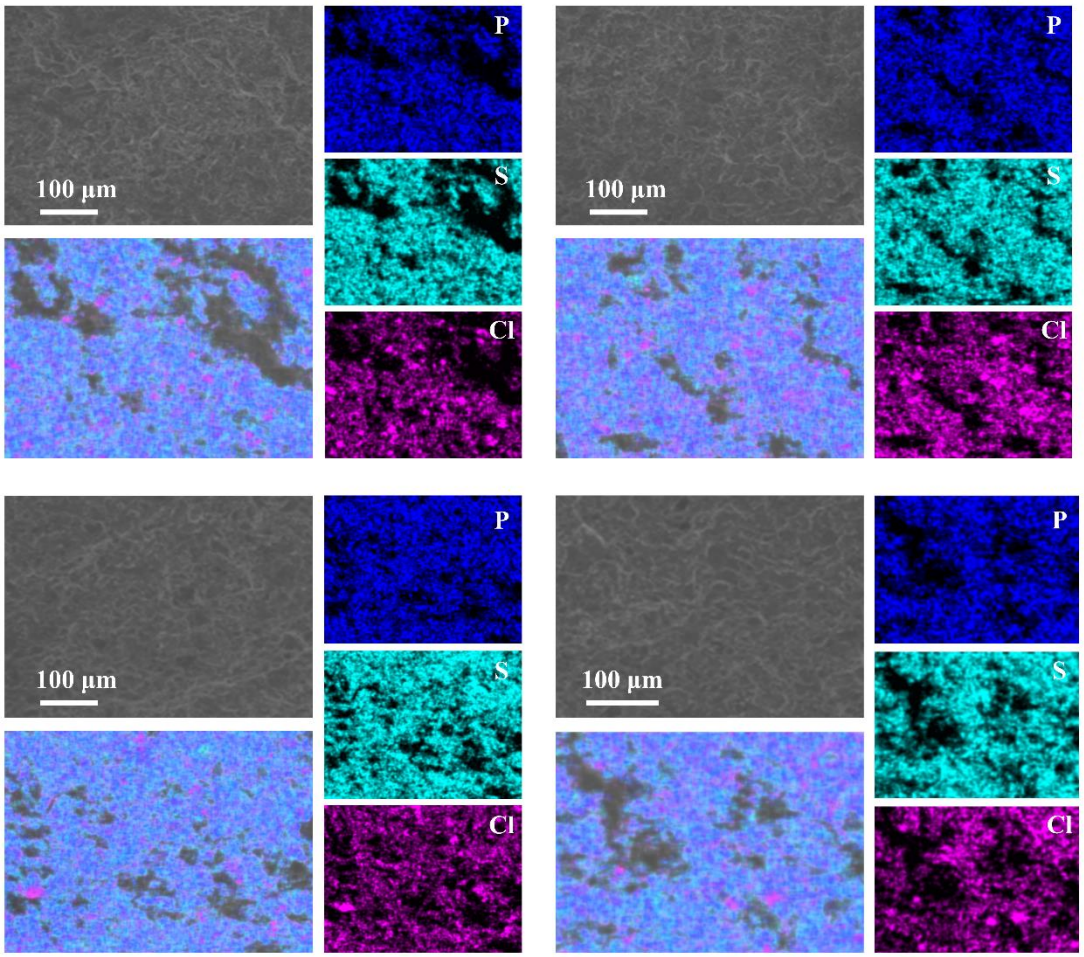

Fig. S42 SEM & EDS observations of vertical section of LPSC electrolyte pellet after cycling from different positions.

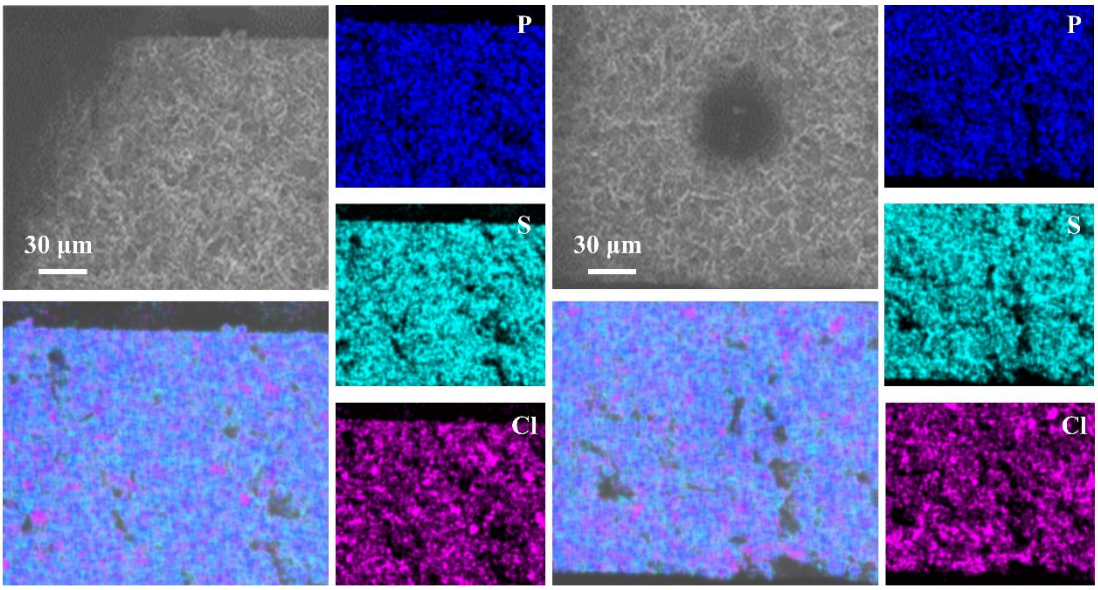

Fig. S43 SEM & EDS observations of vertical section of LPSC electrolyte side layer within Li/LPSC/8S-2O/LPSC/Li symmetric cell from different positions after cycling.

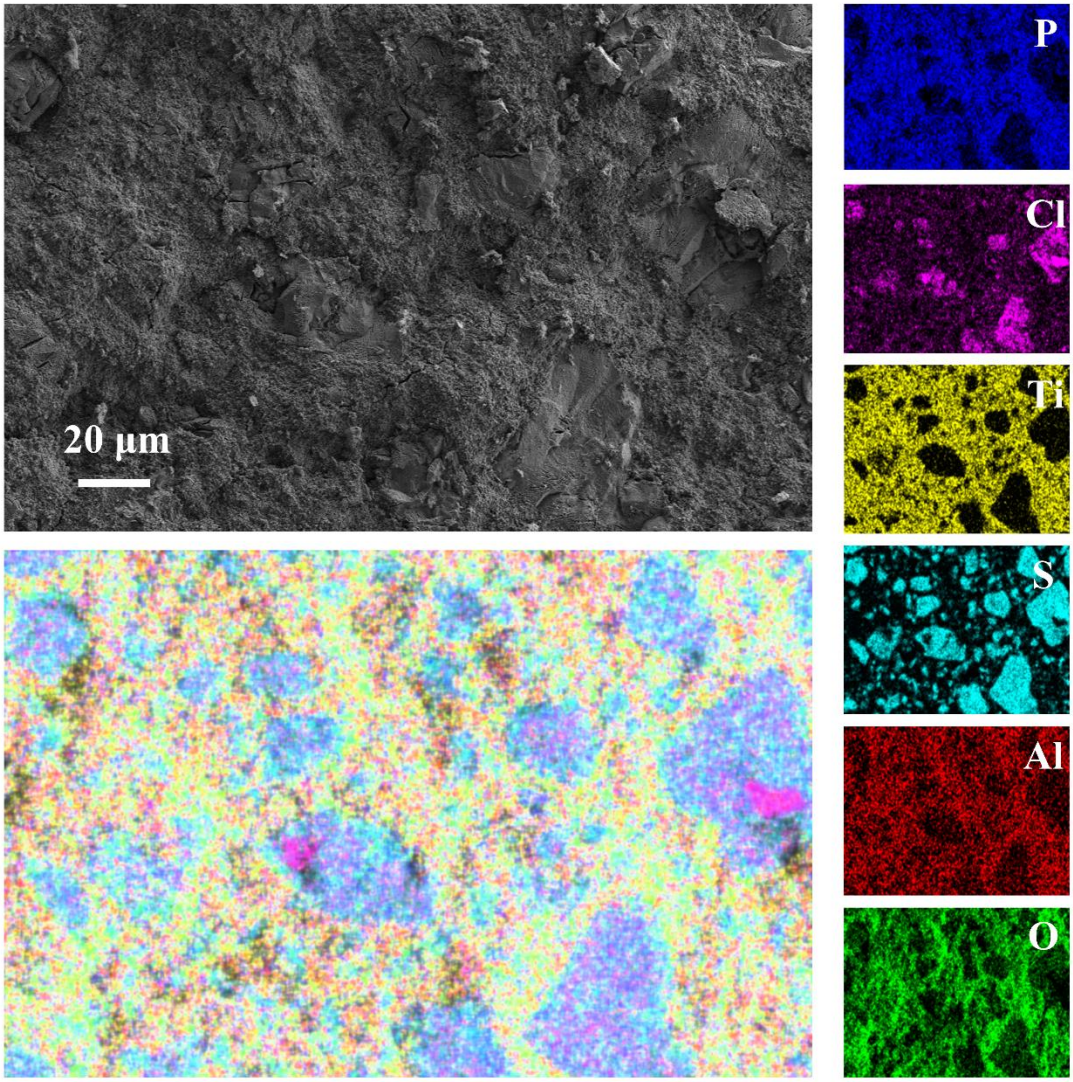

Fig. S44 SEM & EDS observations of LPSC/5S-5O interface within Li/LPSC/5S-5O/LPSC/Li symmetric cell after cycling.

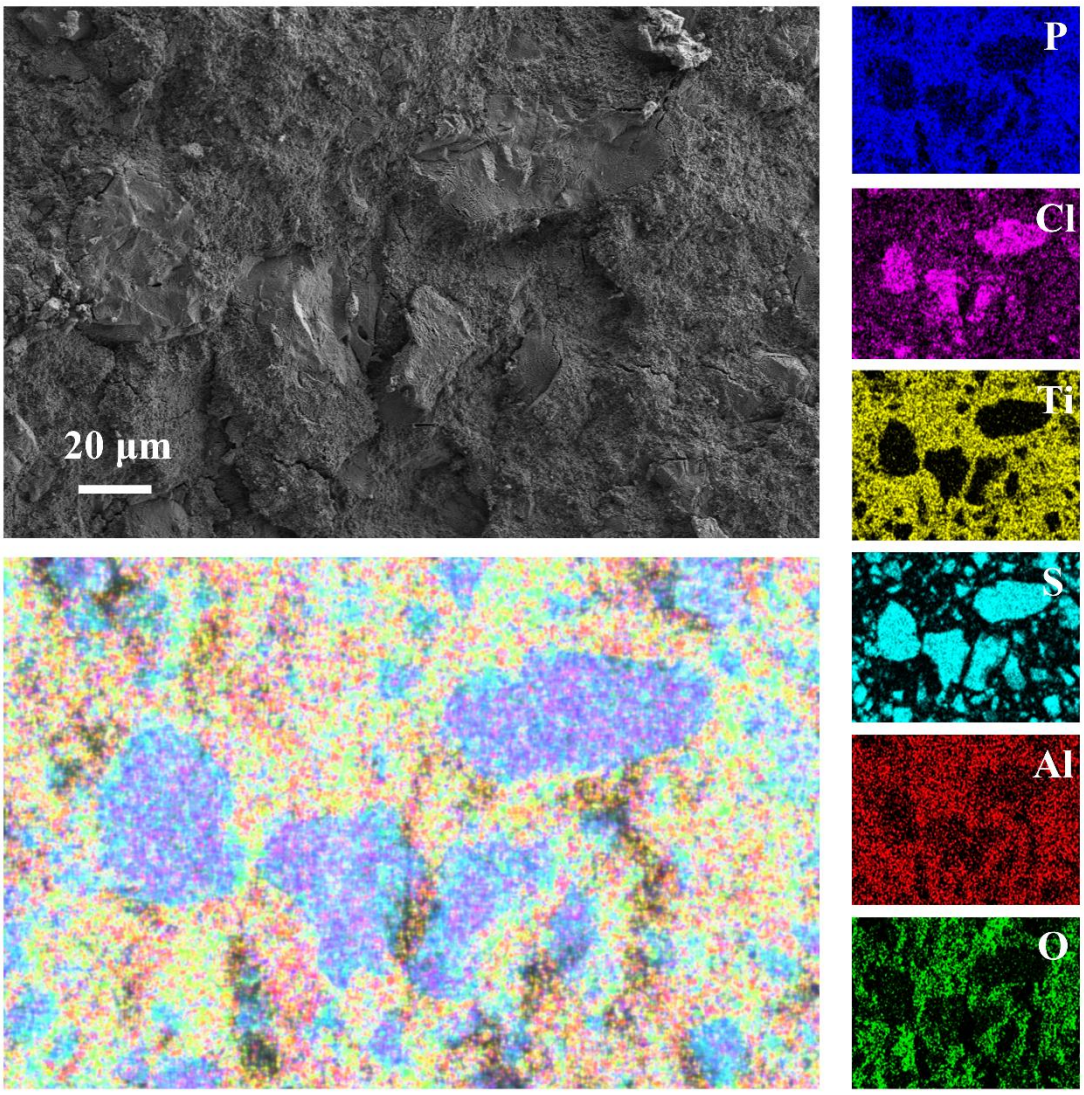

Fig. S45 SEM & EDS observations of LPSC/6S-4O interface within Li/LPSC/6S-4O /LPSC/Li symmetric cell after cycling.

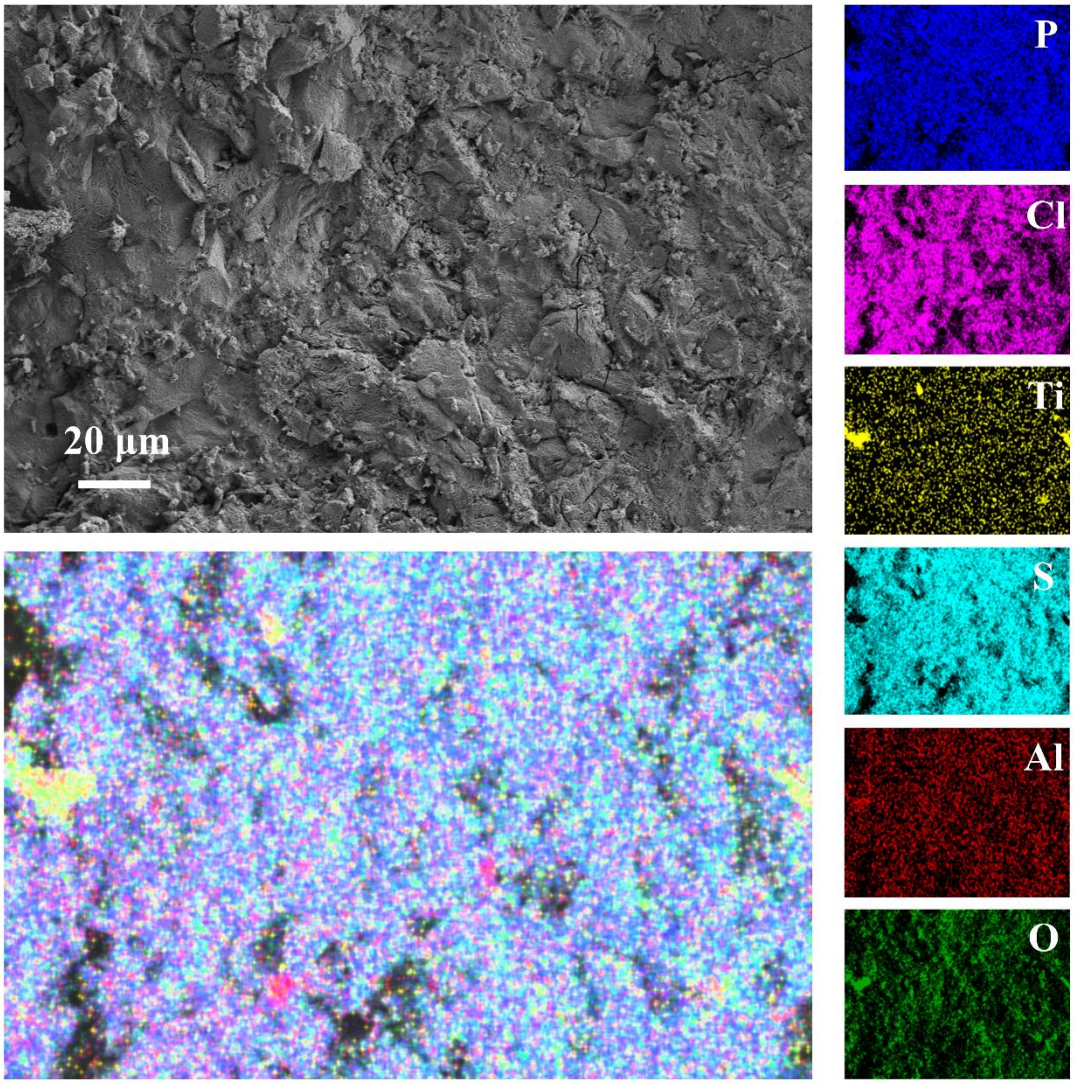

Fig. S46 SEM & EDS observations of LPSC/7S-3O interface within Li/LPSC/7S-3O /LPSC/Li symmetric cell after cycling.

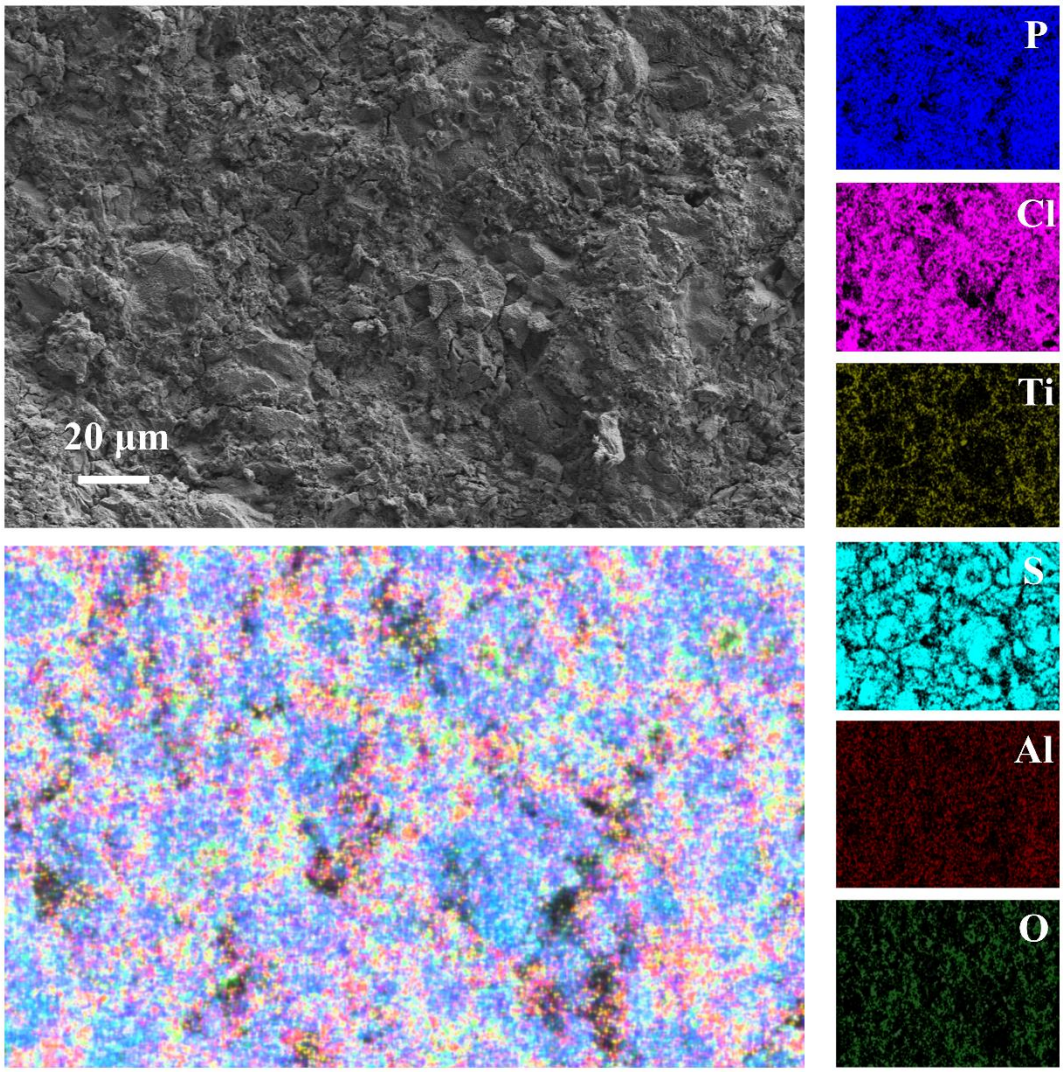

Fig. S47 SEM & EDS observations of LPSC/9S-1O interface within Li/LPSC/9S-1O /LPSC/Li symmetric cell after cycling.

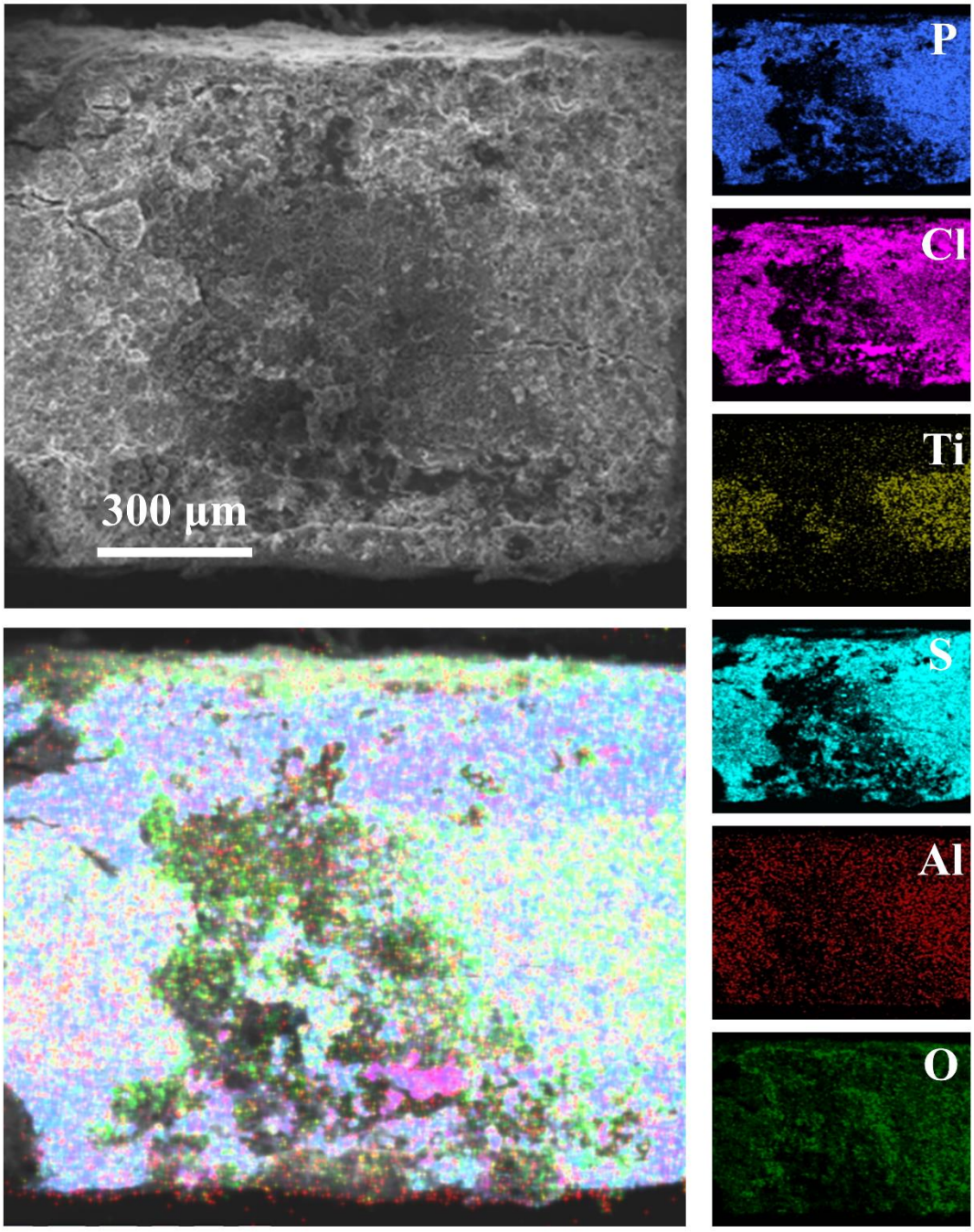

Fig. S48 SEM & EDS observations of cross section of LPSC/8S-2O/LPSC electrolyte pellet after the CCD test to 4.6 mA cm^{-2}.

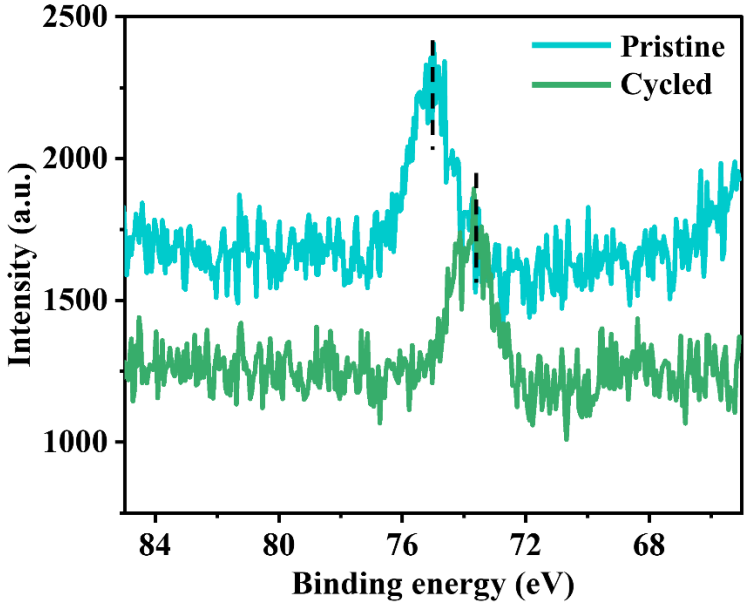

Fig. S49 XPS analysis for Al 2p of LPSC/8S-2O interface within pristine and cycled LPSC/8S-2O/LPSC electrolyte pellet after removal of Li anodes.

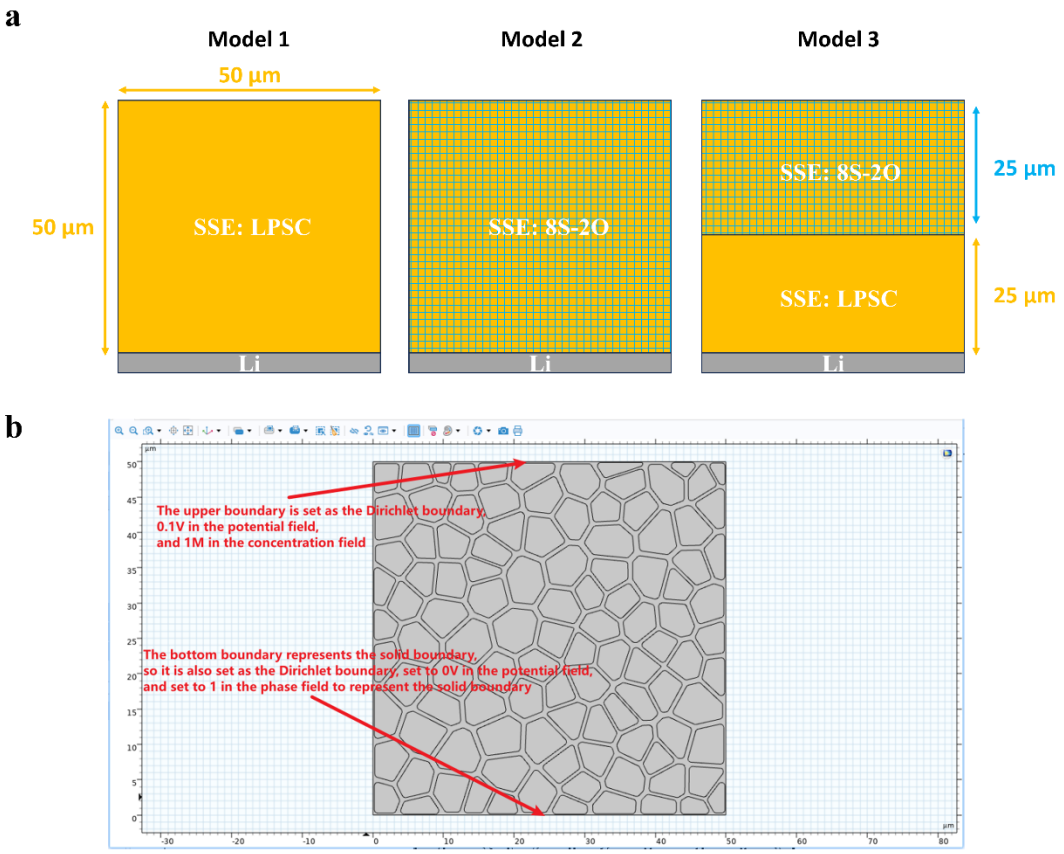

Fig. S50 (a) Schematic illustration of 3 kinds of models for Phase-field simulation and (b) the detailed setting of boundary conditions.

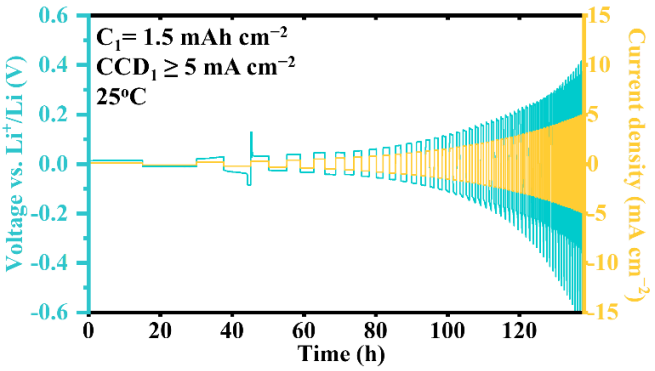

Figure S51 CCD measurements using capacity-constant mode with capacities of 1.5 mAh cm^{-2}.

Description: During the first few cycles, the sudden increase and drop of voltages could be observed, followed by the recovery phenomena, which conform to Ohm's law in subsequent cycles. Such voltage fluctuation and recovery, which are similar to CCD measurements using time-constant mode in Fig. 3a and S30-S36, could be ascribed to comprehensive results of in-situ consumption of Li dendrites and anodic interfacial creep, and the short circuit could be excluded. And evident growths of overpotential at high current density could also attribute to Li creep during high areal capacity of Li plating/stripping.

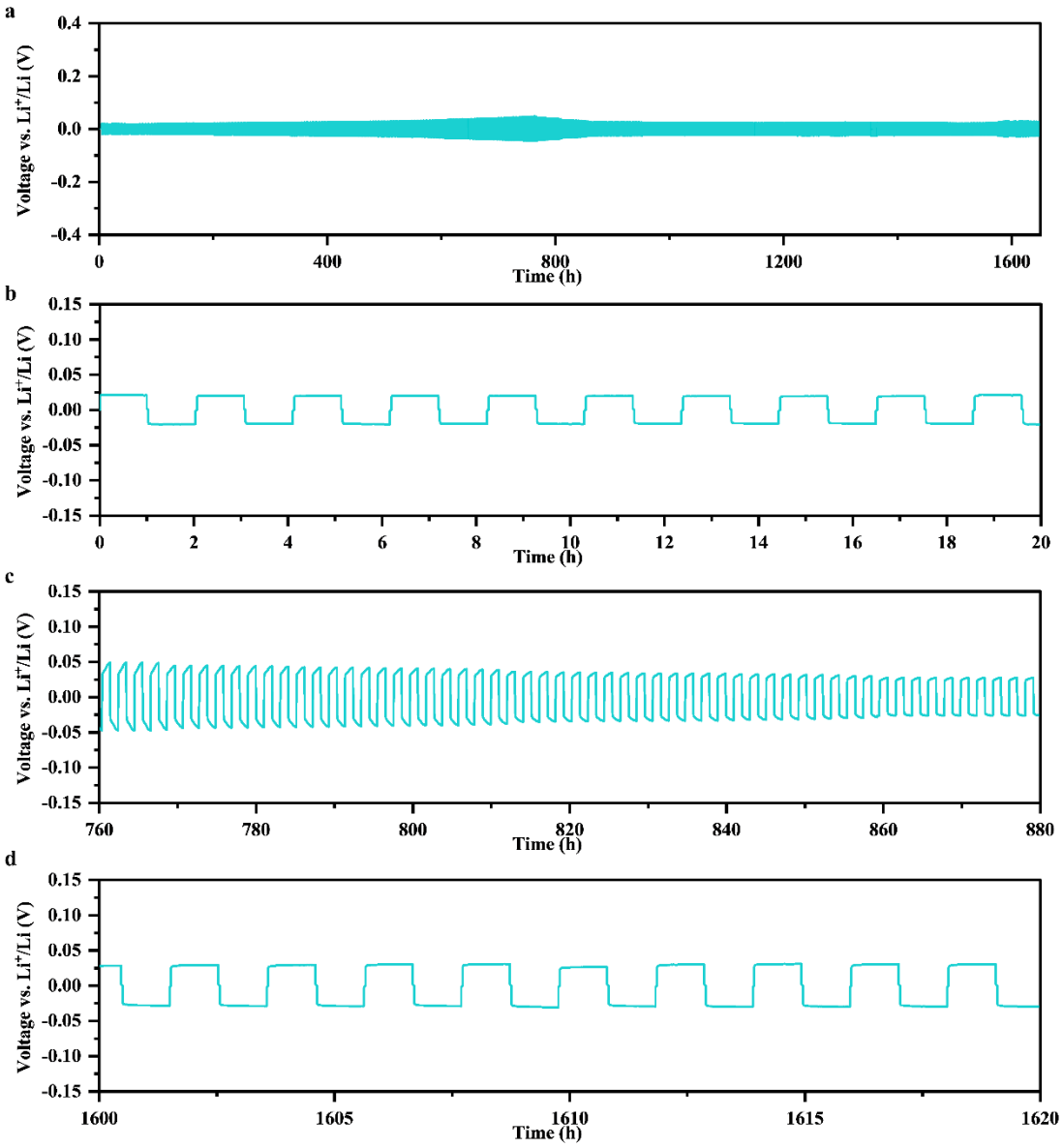

Fig. S52 (a) Long-cycle performance of Li/LPSC/8S-2O/LPSC/Li symmetric cell at current density of 0.5 mA cm^{-2}. The depictions of polarization curves from (b) 0 to 20 h, (c) 760 to 880 h, and (d) 1600 to 1620 h for Li/LPSC/8S-2O/LPSC/Li symmetric cell at current density of 0.5 mA cm^{-2}.

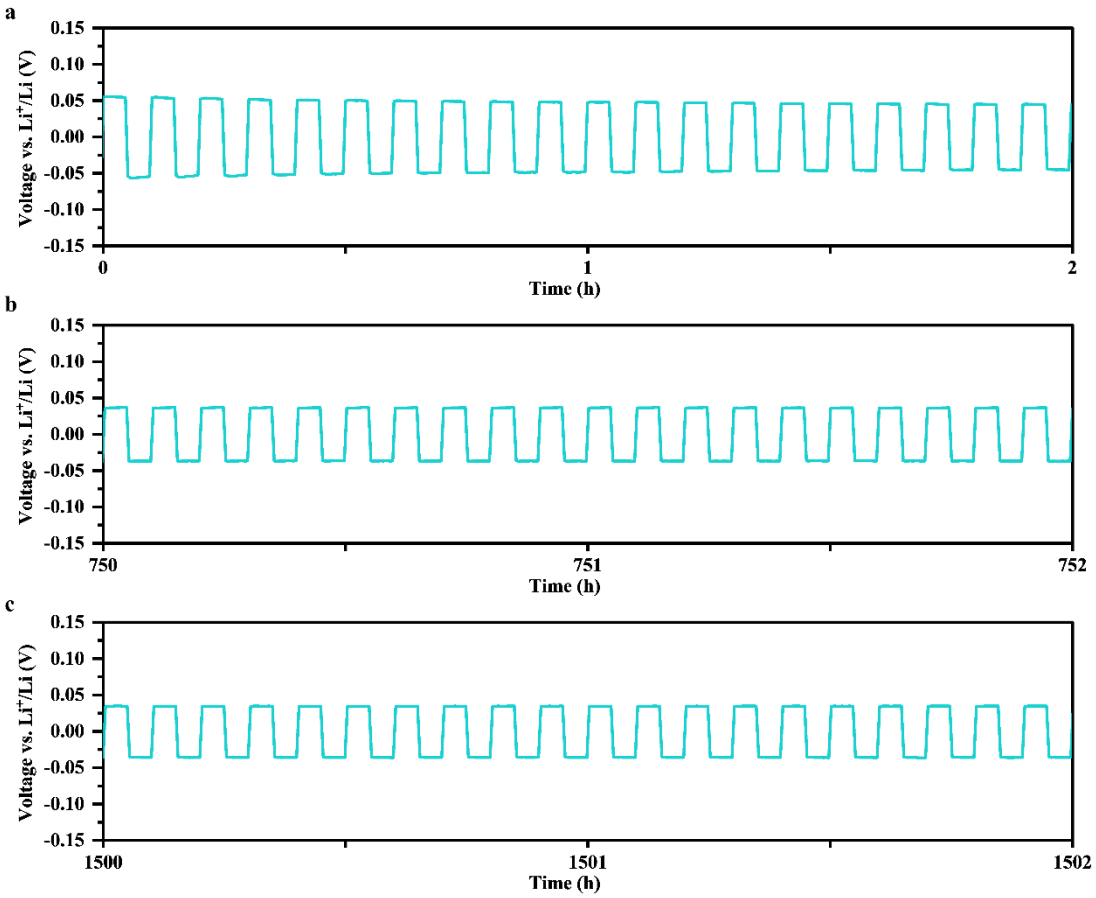

Fig. S53 The depictions of polarization curves from (a) 0 to 2 h, (b) 750 to 752 h, and (c) 1500 to 1502 h for Li/LPSC/8S-2O/LPSC/Li symmetric cell at current density of 10 mA cm^{-2}.

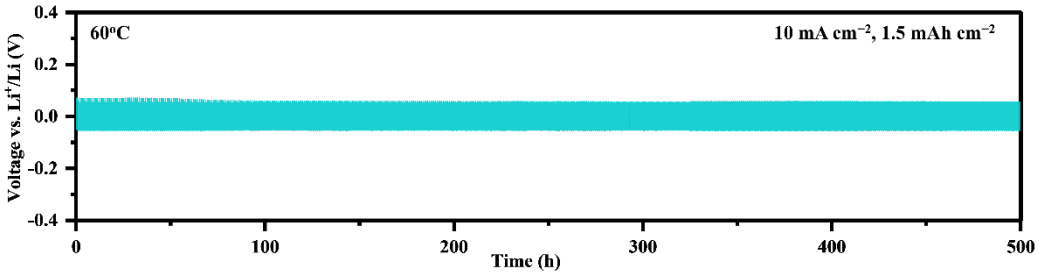

Figure S54. Long-cycle performance of Li/LPSC/8S-2O/LPSC/Li symmetric cell at current density of 10 mA cm^{-2}.

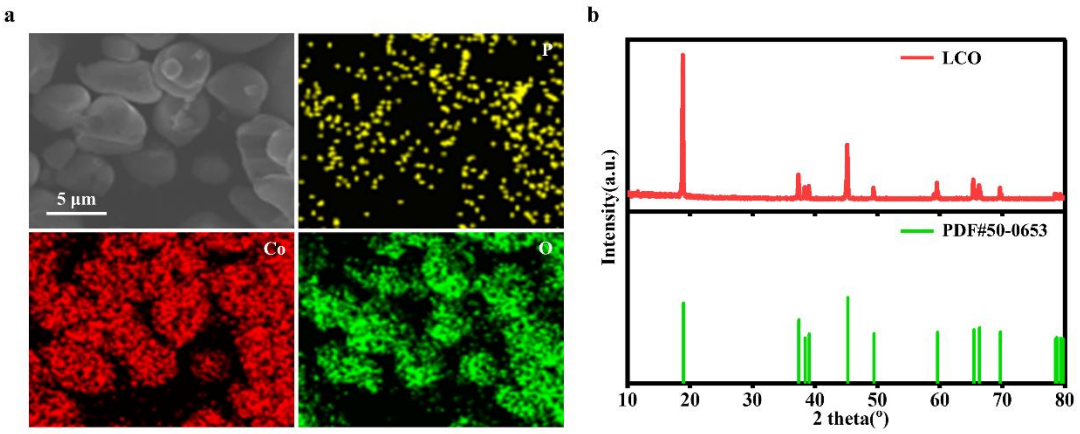

Figure S55. (a) The SEM&EDS characterizations and (b) XRD pattern of Li_3PO_4@LCO cathodes.

Description: The average particle size is around 5 μm through SEM observation and the corresponding EDS results indicate the uniform distributions of P, O and Co elements. The XRD pattern of LCO could also be detected with no visible impurity. Hence, the LCO with uniform Li_3PO_4 coating layer guarantees its high intrinsic and interfacial stability within ASSLMBs.

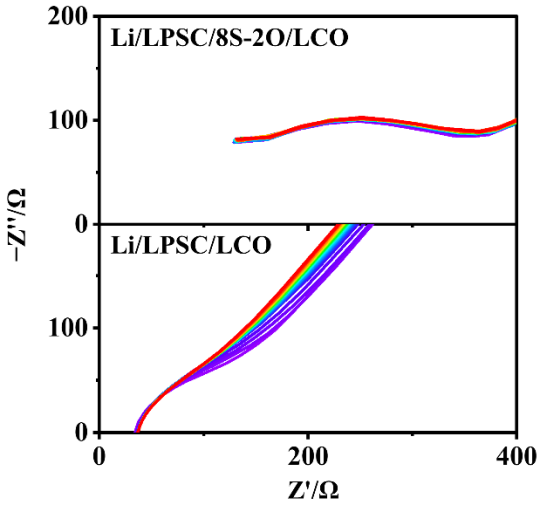

Fig. S56 The in-situ GEIS for Li/LPSC/8S-2O/LCO and Li/LPSC/LCO ASSLMBs during the charge process at 0.1C.

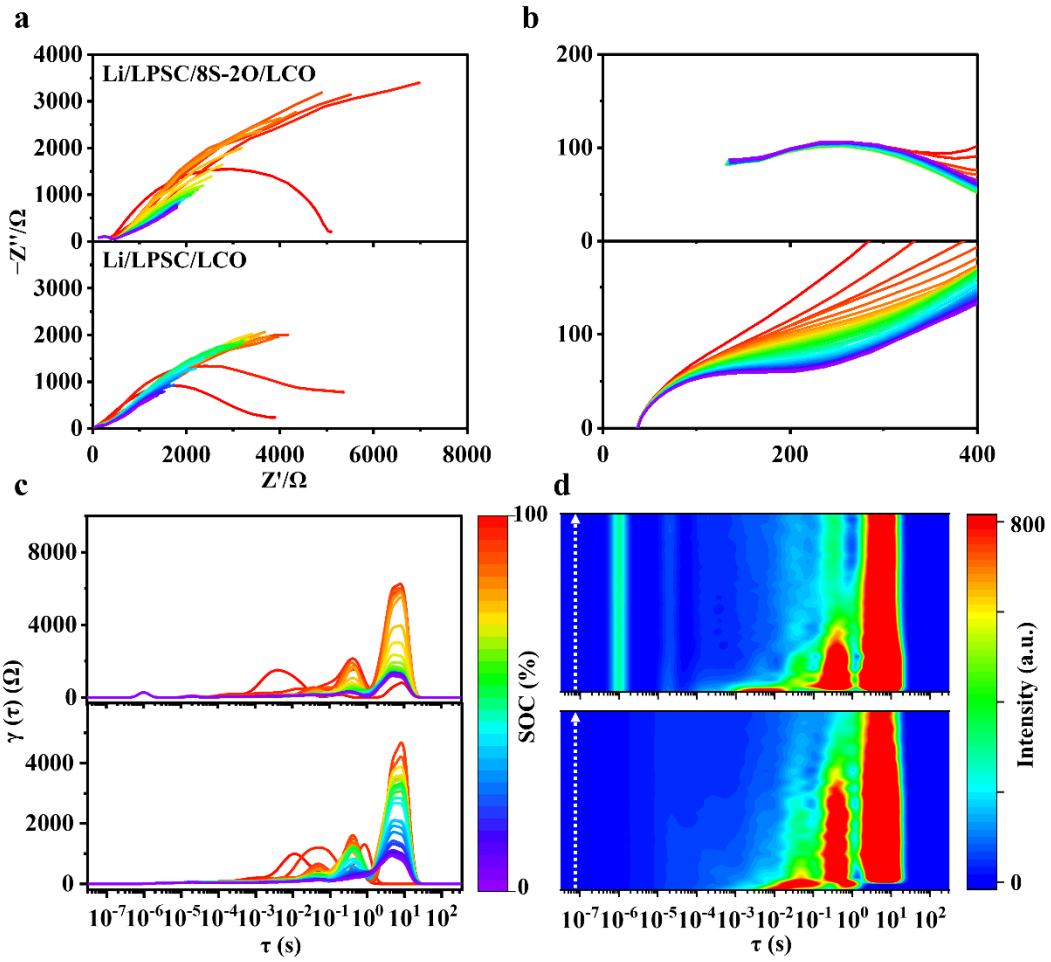

Fig. S57 (a, b) The in-situ GEIS and (c) DRT analyses for Li/LPSC/8S-2O/LCO and Li/LPSC/LCO ASSLMBs during the discharge process at 0.1C, accompanied with (d) corresponding 2D intensity color map.

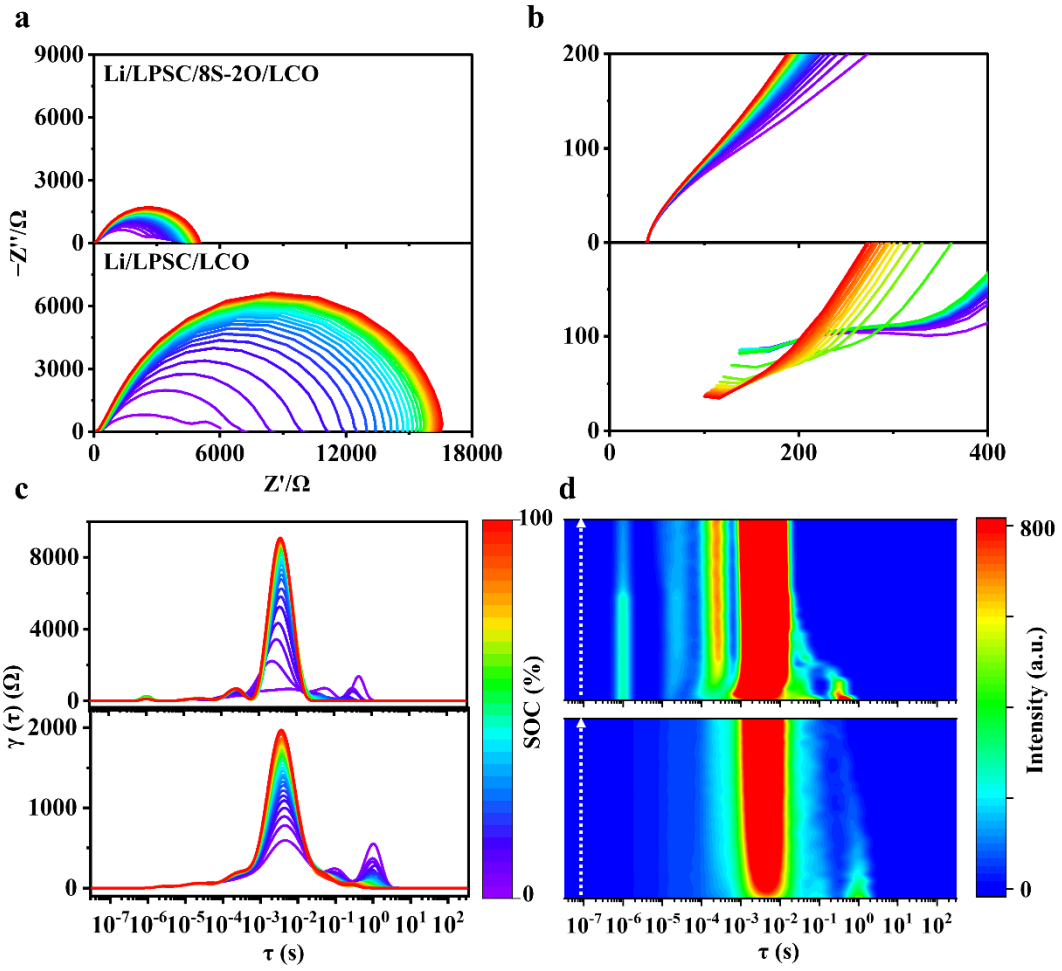

Fig. S58 (a, b) The in-situ GEIS and (c) DRT analyses for Li/LPSC/8S-2O/LCO and Li/LPSC/LCO ASSLMBs during the charge process at 0.2C, accompanied with (d) corresponding 2D intensity color map.

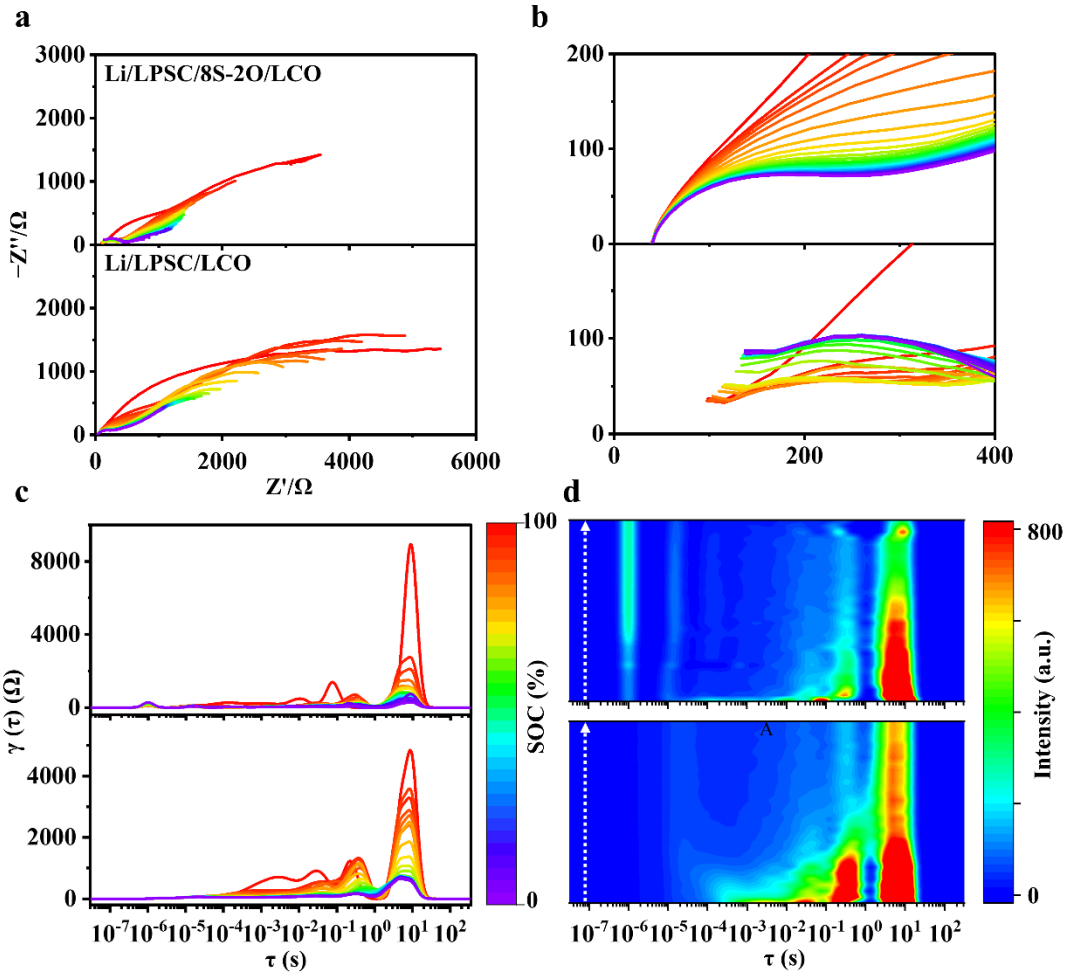

Fig. S59 (a, b) The in-situ GEIS and (c) DRT analyses for Li/LPSC/8S-2O/LCO and Li/LPSC/LCO ASSLMBs during the discharge process at 0.2C, accompanied with (d) corresponding 2D intensity color map.

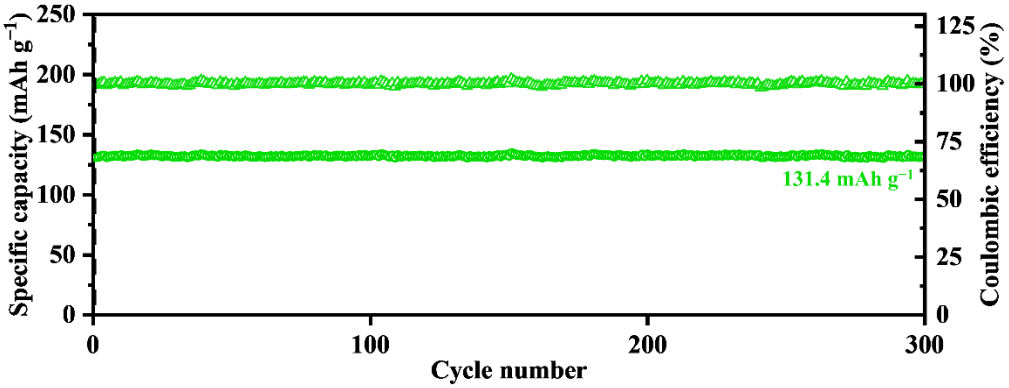

Figure S60. long cycling performance at 1C of Li-In/LPSC/LCO ASSLMBs at RT, where 1C=160 mA g^{-1} and the mass loading is 8 mg cm^{-2}.

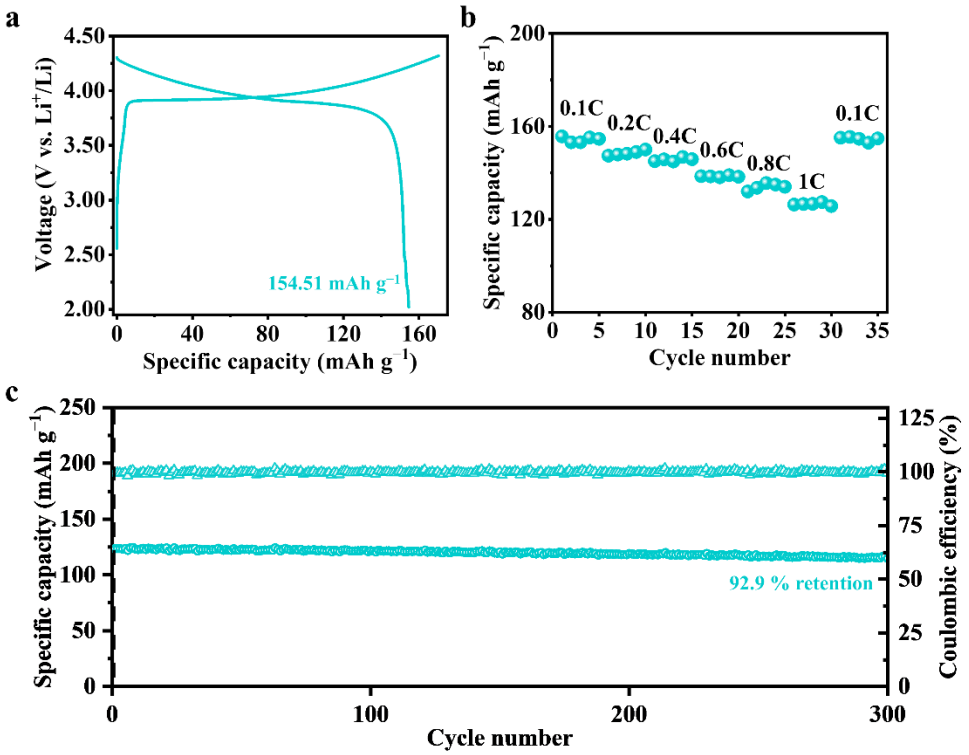

Figure S61. (a) The charge-discharge curves at initial cycle at 0.1C, (b) rate performance and (c) long cycling performance at 1C of Li/8S-2O/LCO ASSLMBs at RT, where 1C=160 mA g^{-1} and the mass loading is 10 mg cm^{-2}.

Table S1. The detailed parameters involved in phase-field simulation in this work.

	Model 1	Model 2	Model 3
α	0.5	0.5	0.5
R	8.314[J/mol/K]	8.314[J/mol/K]	8.314[J/mol/K]
T	297.15[K]	297.15[K]	297.15[K]
L_σ	5×10^{-6}[m^3/J/s]	5×10^{-6}[m^3/J/s]	5×10^{-6}[m^3/J/s]
L_η	0.5[1/s]	0.5[1/s]	0.5[1/s]
F	96500[C/mol]	96500[C/mol]	96500 [C/mol]
c_{Li^+}	1000[mol/m^3]	1000[mol/m^3]	1000[mol/m^3]
δ	0.1	0.1	0.1
σ_{Li}	3.73×10^{-9} S cm^{-1}	1.91×10^{-9} S cm^{-1}	1.91×10^{-9} S cm^{-1} (upper half) 3.73×10^{-9} S cm^{-1} (lower half)
σ_e	0.5×10^{-13}	0.5×10^{-13}	0.5×10^{-13}
W	15×10^5[J/m^3]	15×10^5[J/m^3]	15×10^5[J/m^3]
κ_0	7×10^{-10}[J/m]	7×10^{-10}[J/m]	7×10^{-10}[J/m]
D_{Li}	1×10^{-11}m^2/s	1×10^{-11}m^2/s	1×10^{-11}m^2/s

Table S2. Raman peaks assignment of LPSC electrolyte within composite cathodes in ASSLB with Li_2S as reference.

Frequency	Assignment	Compound	ref
~195 cm^{-1}	PS_4^{3-}	LPSC	5-7
~272 cm^{-1}	δ_{def}(S-P-S) in PS_4^{3-}	LPSC	5-7
~315 cm^{-1}	A_{1g} mode	LATP	8
~354 cm^{-1}	E_g mode	LATP	8
~425 cm^{-1}	$\nu_s(PS_4^{3-})$ in PS_4^{3-}	LPSC	5-7
~570 cm^{-1}	PS_4^{3-}	LPSC	5-7
~600 cm^{-1}	PS_4^{3-}	LPSC	5-7
~383 cm^{-1}	T_{2g} phonon mode	Li_2S	5-7
~1008 cm^{-1}	$\nu_s(PO_4^{3-})$ in PO_4^{3-}	LATP	8
~1094 cm^{-1}	$\nu_{as}(PO_4^{3-})$ in PO_4^{3-}	LATP	8

Table S3. The calculation results of Ea and Ea' for LPSC-LATP composite electrolytes based on the Arrhenius equation.

Samples	Fitting slope (SSEs)	E_a [eV]	Fitting slope (gb2)	E_a' [eV]
10S-0O	−3.745	0.323	--	--
9S-1O	−3.963	0.342	--	--
8S-2O	−3.872	0.334	--	--
7S-3O	−5.541	0.478	−7.700	0.664
6S-4O	-5.930	0.512	−7.227	0.624
5S-5O	-6.216	0.536	−6.390	0.551
LATP	−3.716	0.321	−6.467	0.558

Table S4. The temperature-dependent EIS measurements of LPSC pellet.

Temperature [K]	R_{SSE} [Ω]	σ_{SSE} [mS cm^{-1}]	In(σT)
343.15	3.49	24.85	2.14
333.15	4.59	18.90	1.84
323.15	6.24	13.88	1.50
313.15	8.90	9.74	1.12
303.15	12.32	7.03	0.76
298.15	15.34	5.65	0.52
293.15	19.48	4.45	0.27

Table S5. The temperature-dependent EIS measurements of LATP pellet.

Temperature [K]	R_{SSE} [Ω]	σ_{SSE} [mS cm^{-1}]	In(σT)
343.15	11.63	4.83	0.51
333.15	13.19	4.26	0.35
323.15	19.48	2.89	−0.07
313.15	26.56	2.12	−0.41
303.15	37.57	1.50	−0.79
298.15	48.08	1.17	−1.05
293.15	60.68	0.93	−1.30

Table S6. XPS binding energies with attributed species of LPSC/8S-2O interface within pristine and cycled LPSC/8S-2O/LPSC electrolyte pellet after removal of Li anodes.

Spectra details	Binding energy [eV]	Attributed species
2p	161.54eV ($2p_{1/2}$) 160.33 eV ($2p_{3/2}$)	PS_4^{3-}
Cl 2p	199.26 eV ($2p_{1/2}$) 197.66 eV ($2p_{3/2}$)	Cl^-
Ti 2p	465.77eV($2p_{1/2}$) 460.08 eV($2p_{3/2}$)	Ti^{4+}
Ti 2p	464.81eV ($2p_{1/2}$) 459.03 eV ($2p_{3/2}$)	Ti^{3+}
O 1s	531.25 eV	O^{2-}(LATP)
	530.25 eV	Ti_2O_3

Table S7. Anodic interfacial stability based on SSEs in ASSLMBs between previous work and ours.

Methods	SSE System	Cell Structure	CCD (mA/cm^2)	Current Density (mA/cm^2)/life (h)	Rate /life (h)	Initial capacity (mAh/g)	Final capacity (mAh/g)	Ionic conductivity(mS/cm)
infiltration	LPS	Li/LiFSI-DME-LGPS[9]	2	0.3/350	0.3C/50	120	~116	0.26
infiltration	LGPS	Li/LiTFSI-Mg(TFSI)$_2$-DME-LGPS[10]	1.3	0.2/140	~0.17C/120	~600	400.6	3
multilayer	LGPS	Li/LiH$_2$PO$_4$/LGPS[11]	-	0.1/950	0.1C/500	131.1	113.7	3
multilayer	LPSC	Li/LiTFSI-PPC/LPSC[12]	-	0.5/300	1C/900	~130	132.8	2.44
multilayer	LPSC	Li/Li$_3$Sb-LiF/LPSC[13]	1.8	2/1472	0.1C/100	530	396	2
multilayer	LPSC	Li/ Nb2O5 @CNT/L	1.2	0.1/1000	1C/7000	110	80	-

		PSC[14]						
multilayer	LPSC	Li/Li7N2I-Mg/LPSC[15]	4	4/600	0.5C/350	191.6	147.0	-
multilayer	LPSC	Li/Gr/LPSC/LGPS[16]	0.25	0.25/1500	1.5C/2000	150	80	-
multilayer	LPSC	Li/Li_3N-LiF/LPSC[17]	3.3	0.5/1200	1C/500	121	87.67	-
multilayer	LPS	Li/Li_3N-LiF/LPS[18]	3	1/220	0.3/50	101.3	101.6	-
multilayer	LPS	Li/Gr-LPS/LPS[19]	1.3	-	~0.1C/80	~170	~50	2.01
multilayer	LPSC	Li/LPSC/LTLC[20]	1.52	0.5/500	0.5C/200	154	134.4	1.76
multilayer	LPSC	Li-LiF-organic layer/LPSC[21]	1.9	0.3/1200h	0.5C/100	107	81	2.59
Doping	LPS	Li/LPS-0.05Mo[22]	0.96	0.5/50	-	-	-	2.5
Doping	LPS	Li/$Li_{3.2}P_{0.8}Sn_{0.2}S_4$[23]	-	0.1/600	0.1C/60	118.4	91.1	1.21
Doping	LPSC	Li/Li_3N-	1.52	0.5/100	0.1C	95.1	82.3	1.3

		Li_6PS_5Cl [24]		0	/100			
Doping	LPSB	Li/ZnO-Li_6PS_5Cl [25]	0.58	0.78/140	0.1C /-	94.8	-	1
Doping	LPSB	Li/O-LPSB[26]	0.9	0.1/550	0.8C /175	47.4	47.1	1.8
Doping	LPSC	Li/LPSC$l_{0.3}F_{0.7}$[27]	-	1.27/1000	0.1C /50	103	97.9	0.71
Refining	LPSC	Li/WM-LPSC[28]	2.6	1/800	0.1C /40	175	165	1.8
Refining	LPSCB	Li/LPSCB[29]	3.8	0.5/1000	1C/1000	99	80	14.1
Refining	LPSCB	Li/LPSCB[29]	3.8	1/500	1C/1000	99	80	14.1
Refining	LPSCB	Li/LPSCB[29]	3.8	3/160	1C/1000	99	80	14.1
Compositing	LPSC	Li/LiF-LPSC[30]	2.2	0.5/1400	0.1C /200	106.14	60	3.4
Alloying	LPSC	Li-Ag/LPSC[31]	1.5	1/1000	5C/4000	60	54	-
This work	LPSC	Li/LPSC/8S-2O	4.4	10/1600	1C/1200	127.8	109.4	2

3. References in supporting information

1. G. Kresse and D. Joubert, *Phys Rev B*, 1999, **59**, 1758-1775.
2. J. P. Perdew, K. Burke and M. Ernzerhof, *Physical Review Letters*, 1996, **77**, 3865-3868.
3. S. Grimme, J. Antony, S. Ehrlich and H. Krieg, *The Journal of Chemical Physics*, 2010, **132**.
4. H. K. Tian, Z. Liu, Y. Z. Ji, L. Q. Chen and Y. Qi, *Chem Mater*, 2019, **31**, 7351-7359.

5. Y. D. Zhou, C. Doerrer, J. Kasemchainan, P. G. Bruce, M. Pasta and L. J. Hardwick, *Batteries & Supercaps*, 2020, **3**, 647-652.
6. L. Z. Sang, R. T. Haasch, A. A. Gewirth and R. G. Nuzzo, *Chem Mater*, 2017, **29**, 3029-3037.
7. M. Tachez, J. P. Malugani, R. Mercier and G. Robert, *Solid State Ionics*, 1984, **14**, 181-185.
8. S. Ghosh, C. Sudarshan and C. Sudakar, *Journal of Applied Physics*, 2023, **133**, 245106.
9. X. L. Fan, X. Ji, F. D. Han, J. Yue, J. Chen, L. Chen, T. Deng, J. J. Jiang and C. S. Wang, *Sci Adv*, 2018, **4**, eaau9245.
10. H. Wan, S. Liu, T. Deng, J. Xu, J. Zhang, X. He, X. Ji, X. Yao and C. Wang, *Acs Energy Lett*, 2021, **6**, 862-868.
11. Z. H. Zhang, S. J. Chen, J. Yang, J. Y. Wang, L. L. Yao, X. Y. Yao, P. Cui and X. X. Xu, *Acs Appl Mater Inter*, 2018, **10**, 2556-2565.
12. Y. Chen, W. W. Li, C. Z. Sun, J. Jin, Q. Wang, X. D. Chen, W. P. Zha and Z. Y. Wen, *Adv Energy Mater*, 2021, **11**, 2002545.
13. Y. Zhao, J. Liu, Y. Zhang, H. Zhu, J. Yang, Y. Nuli and J. Wang, *Energy Storage Materials*, 2024, **69**, 103432.
14. L. Song, R. Li, H. Zhu, Z. Li, G. Liu, Z. Peng, X. Fan and X. Yao, *Adv Mater*, 2024, **36**, 2400165.
15. Z. Wang, J. Xia, X. Ji, Y. Liu, J. Zhang, X. He, W. Zhang, H. Wan and C. Wang, *Nature Energy*, 2024, **9**, 251-262.
16. L. Ye and X. Li, *Nature*, 2021, **593**, 218-222.
17. Q. Gao, D. Wu, Z. Wang, P. Lu, X. Zhu, T. Ma, M. Yang, L. Chen, H. Li and F. Wu, *Energy Storage Materials*, 2023, **63**, 103007.
18. X. Ji, S. Y. Hou, P. F. Wang, X. Z. He, N. Piao, J. Chen, X. L. Fan and C. S. Wang, *Adv Mater*, 2020, **32**, 2002741.
19. X. Xing, Y. Li, S. Wang, H. Liu, Z. Wu, S. Yu, J. Holoubek, H. Zhou and P. Liu, *Acs Energy Lett*, 2021, **6**, 1831-1838.
20. S. Xu, X. Cheng, S. Yang, Y. Yin, X. Wang, Y. Zhang, D. Ren, Y. Sun, X. Sun, H. Yao and Y. Yang, *Adv Mater*, 2024, **36**, 2310356.
21. Y. Shi, Q. Li, X. Hu, Y. Liao, W. Li, Y. Xu, B. Zhao, J. Zhang and Y. Jiang, *Nano Energy*, 2024, **120**, 109150.
22. Z. Wang, Y. Jiang, J. Wu, Y. Jiang, W. Ma, Y. Shi, X. Liu, B. Zhao, Y. Xu and J. Zhang, *Nano Energy*, 2021, **84**, 105906.
23. F. Zhao, S. H. Alahakoon, K. Adair, S. Zhang, W. Xia, W. Li, C. Yu, R. Feng, Y. Hu, J. Liang, X. Lin, Y. Zhao, X. Yang, T.-K. Sham, H. Huang, L. Zhang, S. Zhao, S. Lu, Y. Huang and X. Sun, *Adv Mater*, 2021, **33**, 2006577.
24. Y. Liu, H. Su, M. Li, J. Xiang, X. Wu, Y. Zhong, X. Wang, X. Xia, C. Gu and J. Tu, *J Mater Chem A*, 2021, **9**, 13531-13539.
25. T. Chen, L. Zhang, Z. X. Zhang, P. Li, H. Q. Wang, C. Yu, X. L. Yan, L. M. Wang and B. Xu, *Acs Appl Mater Inter*, 2019, **11**, 40808-40816.
26. Z. X. Zhang, L. Zhang, X. L. Yan, H. Q. Wang, Y. Y. Liu, C. Yu, X. T. Cao, L. van Eijck and B. Wen, *Journal of Power Sources*, 2019, **410**, 162-170.

27. F. P. Zhao, Q. Sun, C. Yu, S. M. Zhang, K. Adair, S. Z. Wang, Y. L. Liu, Y. Zhao, J. W. Liang, C. H. Wang, X. N. Li, X. Li, W. Xia, R. Y. Li, H. Huang, L. Zhang, S. Q. Zhao, S. G. Lu and X. L. Sun, *Acs Energy Lett*, 2020, **5**, 1035-1043.
28. Y. Wang, H. Hao, K. G. Naik, B. S. Vishnugopi, C. D. Fincher, Q. Yan, V. Raj, H. Celio, G. Yang, H. Fang, Y.-M. Chiang, F. A. Perras, P. Jena, J. Watt, P. P. Mukherjee and D. Mitlin, *Adv Energy Mater*, 2024, **14**, 2304530.
29. Y. Liu, H. Su, Y. Zhong, M. Zheng, Y. Hu, F. Zhao, J. T. Kim, Y. Gao, J. Luo, X. Lin, J. Tu and X. Sun, *Adv Energy Mater*, 2024, **14**, 2400783.
30. H. Liu, W. Jiang, W. Chen, Q. Lin, S. Ren, Y. Su, R. Tong and Y. Zhang, *J Mater Chem A*, 2024, **12**, 3575-3579.
31. S. Zhang, J. Chen, C. Zhu, Q. Liu, Q. Li, R. Liu, X. Jiang, Y. Yan, S. Sun, L. Yin and R. Wang, *Acs Nano*, 2023, **17**, 24290-24298.